PREPLANETARY NEBULAE: A *HUBBLE SPACE TELESCOPE* IMAGING SURVEY AND A NEW MORPHOLOGICAL CLASSIFICATION SYSTEM

RAGHVENDRA SAHAI,[1] MARK MORRIS,[2] CARMEN SÁNCHEZ CONTRERAS,[3] AND MARK CLAUSSEN[4]

ABSTRACT

Using the *Hubble Space Telescope* (*HST*), we have carried out a survey of candidate preplanetary nebulae (PPNs). We report here our discoveries of objects having well-resolved geometric structures, and we use the large sample of PPNs now imaged with *HST* (including previously studied objects in this class) to devise a comprehensive morphological classification system for this category of objects. The wide variety of aspherical morphologies which we have found for PPNs are qualitatively similar to those found for young planetary nebulae (PNs) in previous surveys. We also find prominent halos surrounding the central aspherical shapes in many of our objects; these are direct signatures of the undisturbed circumstellar envelopes of the progenitor AGB stars. Although the majority of these have surface brightness distributions consistent with a constant mass-loss rate with a constant expansion velocity, there are also examples of objects with varying mass-loss rates. As in our surveys of young PNs, we find no round PPNs. The similarities in morphologies between our survey objects and young PNs supports the view that the former are the progenitors of aspherical PNs. This suggests that the primary shaping of a PN does not occur during the PN phase via the fast radiative wind of the hot central star, but significantly earlier in its evolution.

Key words: circumstellar matter — planetary nebulae: general — stars: AGB and post-AGB — stars: mass loss

1. INTRODUCTION

Preplanetary nebulae (PPNs), short-lived transition objects between the AGB and planetary nebula (PN) phases, probably hold the key to understanding how the slowly expanding ($5-15$ km s^{-1}), largely spherical, circumstellar envelopes (CSEs) of AGB stars (Neri et al. 1998) transform into highly aspherical PNs with fast outflows ($\gtrsim100$ km s^{-1}) directed along one or more axes.

We are carrying out a program of multiwavelength imaging and spectroscopic observations of generally young PPNs, using a large (~300), morphologically unbiased sample (Sahai & Sánchez Contreras 2002, 2004), mostly constructed from catalogs of OH/IR stars (evolved, visually faint, mass-losing stars with dense CSEs, showing generally double-peaked OH maser emission). Interferometric maps of the OH emission in many of the objects of this class (e.g., Bowers et al. 1983) show that it typically arises in an extended circular shell of radius $\sim10^{16}$ cm, indicating that substantial AGB mass loss has occurred through a spherical outflow. The *IRAS* spectral energy distributions (SEDs) of a large fraction of these objects indicate a lack of hot dust ($25-12$ μm flux ratio $F_{25}/F_{12} > 1$, implying a lack of dust hotter than about 450 K) and therefore cessation of the dense AGB mass-loss process less than a few hundred years ago.

Here we report on our discoveries of objects with well-resolved geometric structures from our imaging surveys of PPNs carried out using the *Hubble Space Telescope* (*HST*) in its SNAPshot mode. A previous SNAPshot survey providing images of resolved nebulosities in 21 PPNs was carried out by Ueta et al. (2000). We use the large sample (>50) of PPNs now available (which includes previously imaged objects in this class) to devise a new mor-

phological classification system for this category of objects. We also derive post-AGB and AGB mass-loss timescales, as well as dust masses, for our objects. The main focus of this paper is the morphology of PPNs; a more comprehensive statistical analysis which includes results on the unresolved and undetected objects in our surveys is deferred to a future paper.

2. OBSERVATIONS

The images presented in this paper were obtained as part of two SNAPshot survey programs with *HST*. The target lists for these programs were generated by selecting sources from published catalogs of OH/IR stars (te Lintel Hekkert et al. 1988, 1991, 1992; Chengalur et al. 1993; te Lintel Hekkert & Chapman 1996; Hu et al. 1994; Likkel 1989; Sevenster et al. 2001, 1997a, 1997b) which had strong emission (≥0.8 Jy) in the OH maser lines (1665, 1667, and/or 1612 MHz) and with $F_{25}/F_{12} > 1.4$. A small number of additional objects were selected from the compilation of evolved stars with low-resolution *IRAS* spectra by Kwok et al. (1997), subject to the same *IRAS* color criterion as for the OH/IR stars. This subset included carbon-rich (C-rich) objects and class H objects (showing a red continuum with either a 9.7 μm silicate absorption feature or a 11.3 μm PAH emission feature in their LRS spectra).

A 25 μm flux threshold of 25 Jy was then imposed in order to exclude relatively distant objects. This yielded a sample of about 200 objects. The Digitized Sky Survey (DSS) optical images, available from the online databases maintained by the Canadian Astronomy Data Centre, were used to examine a 3×3 arcmin^2 field of view around each object in order to check whether any bright field stars were present very close to our target, which would make their imaging difficult. Objects for which no visual detection could be made on the DSS plates were excluded. The USNO-B.1 and the Guide Star Catalog II (GSC-II) were queried to determine R magnitudes; when these were unavailable, a rough assessment of the R magnitude was made from the DSS images. The remaining sample was divided into 3 mag bins (bright, $R < 13$; medium, $14 < R < 17$; and faint, $R > 17$), and roughly equal

[1] Jet Propulsion Laboratory, California Institute of Technology, MS 183-900, Pasadena, CA 91109, USA.
[2] Department of Physics and Astronomy, UCLA, Los Angeles, CA 90095-1547, USA.
[3] Departamento de Astrofísica Molecular e Infraroja, Instituto de Estructura de la Materia, CSIC, Serrano 121, 28006 Madrid, Spain.
[4] National Radio Astronomy Observatory, 1003 Lopezville Road, Socorro, NM 87801, USA.

numbers of objects were randomly selected from each bin in order to meet the target limitation of 117 objects for the two survey programs, GO 9101 (17 objects) and 9463 (100 objects), described below. A small number of targets which represent the evolutionary phases just preceding and following the PPN phase were also included in these two programs.

Both programs were carried out in the SNAPshot mode of *HST* in which objects are selected from the program source list to fill gaps in the general observational schedule; thus, all objects in the list were not observed. The first survey program, GO 9101, was a pilot survey with the Wide Field Planetary Camera 2 (WFPC2) in which 10/17 objects were imaged. The second, GO 9463, was a more extensive survey in which a total of 58/100 objects were imaged with the Advanced Camera for Surveys (ACS). For GO 9101, we obtained images using the F606W ($\lambda = 0.60$ μm, $\Delta\lambda = 0.123$ μm) and F814W ($\lambda = 0.80$ μm, $\Delta\lambda = 0.149$ μm) filters, with the 800×800 pixel Planetary Camera (PC) of WFPC2, which has a plate scale of $0.0456''$ pixel^{-1}. For GO 9463, we used either the High Resolution Channel (HRC) or the Wide Field Channel (WFC) of the ACS, depending on the optical magnitude of the object. The HRC has a plate scale of $0.025''$ pixel^{-1}, and for objects imaged with this camera, we used a combination of the F606W filter ($\lambda = 0.60$ μm, $\Delta\lambda = 0.123$ μm) and the F814W filter ($\lambda = 0.80$ μm, $\Delta\lambda = 0.149$ μm) for the fainter objects and the F435W filter ($\lambda = 0.43$ μm, $\Delta\lambda = 0.103$ μm) and the F606W filter for the brighter ones. The WFC has a plate scale of $0.050''$ pixel^{-1}, and for objects imaged with this camera, we used a combination of the F606W and F814W filters. We also examined the *HST* archive for additional PPNs which met our *IRAS* color and flux selection criteria (and were not published previously). We found one such object, IRAS 15553-4230 (GO 10627; PI: M. Meixner), which was imaged with the ACS HRC; we have included it in this paper.

Some of the objects from GO 9463 were also imaged as part of our GO 9801 program—a third survey to image optically faint PPN candidates with Camera 1 or 2 of the Near-Infrared Camera and Multi-Object Spectrometer (NICMOS) using two or three of the F110W ($\lambda = 1.1$ μm, $\Delta\lambda = 0.55$ μm), F160W ($\lambda = 1.6$ μm, $\Delta\lambda = 0.4$ μm), and F205W ($\lambda = 2.0$ μm, $\Delta\lambda = 0.6$ μm) filters. The complete results of this survey, which did not yield resolved images of any new PPNs, will be discussed separately; in this paper we utilize the NICMOS images when available for providing additional details on the morphology.

3. RESULTS

We have listed the sources in our survey in Table 1, with their 2MASS coordinates. The images of all resolved objects are shown in Figures 1–30. Optical spectroscopy, allowing the spectral types of the central stars to be determined (either from direct starlight if the central star is visible or from starlight scattered by nebular dust), is not available for all of our objects. However, we have carried out spectroscopic surveys of partially overlapping samples of candidate PPNs selected in the same manner as for our imaging surveys, using the Palomar 60 inch (1.5 m) (Sahai & Sánchez Contreras 2002, 2004) and Keck 10 m telescopes (Sánchez Contreras et al. 2003; C. Sánchez Contreras et al. 2008, in preparation), and we find that the observed objects do not show the rich emission-line spectra characteristic of PNs. For those objects where spectral types have been determined, either by us or by others, the spectral types obtained generally span the B, A, F, and G spectral types, which are the typical spectral types for post-AGB central stars.

The majority of our objects are oxygen-rich (O-rich) due to their selection from OH maser catalogs. Information about the

TABLE 1
SURVEY TARGETS

IRAS Name	R.A. (J2000.0)	Decl. (J2000.0)	Chem.
Preplanetary Nebulae			
01037+1219[a]	01 06 25.98	+12 35 53.0	O
11385−5517.........	11 40 58.81	−55 34 25.8	O
13428−6232	13 46 20.54	−62 47 59.6	...
13557−6442	13 59 28.92	−64 57 18.3	O
15405−4945	15 44 11.06	−49 55 22.1	O
15452−5459	15 49 11.38	−55 08 51.6	O
15553−5230	15 59 11.18	−52 38 41.6	...
16559−2957	16 59 08.22	−30 01 40.3	O
17253−2831	17 28 32.96	−28 33 25.8	O
17347−3139	17 38 00.61	−31 40 55.2	O
17440−3310	17 47 22.72	−33 11 09.3	O
17543−3102	17 57 33.61	−31 03 03.5	O
18276−1431	18 30 30.70	−14 28 57.0	O
18420−0512	18 44 41.65	−05 09 17.0	O
19024+0044	19 05 02.06	+00 48 50.9	O
19134+2131	19 15 35.21	+21 36 34.0	O
19292+1806	19 31 25.37	+18 13 10.3	O
19306+1407	19 32 55.08	+14 13 36.9	C+O
19475+3119	19 49 29.56	+31 27 16.3	O
20000+3239	20 01 59.52	+32 47 32.9	C
22036+5306	22 05 30.29	+53 21 32.8	O
22223+4327	22 24 31.43	+43 43 10.9	C
23304+6147	23 32 44.79	+62 03 49.1	C
Other Objects			
05506+2414[b]........	05 53 43.56	+24 14 44.7	...
17047−5650[c]	17 09 00.93	−56 54 48.0	...
19255+2123[c]........	19 27 44.02	+21 30 03.4	...
21282+5050[c]........	21 29 58.47	+51 04 00.3	...
22568+6141[c]........	22 58 54.89	+61 57 58.0	...

NOTE.—Units of right ascension are hours, minutes, and seconds, and units of declination are degrees, arcminutes, and arcseconds.
[a] Nascent PPN.
[b] Most likely a YSO.
[c] PN.

source chemistry is provided in the descriptions of individual PPNs in § 4.

3.1. *Morphological Classification System*

The PPNs in our survey show a variety of morphologies. We therefore describe a systematic method of classifying these. In this morphological classification system, we have taken care to avoid using criteria that are based on a three-dimensional interpretation of the nebular structures whose two-dimensional projection is observed in our images. The main structural components of PPNs in order of importance are the lobes, the waist, and the halo. Hence, we classify our objects into various morphological classes with the prime discriminant being the lobe structure. The presence or absence of a waist and halo are included as secondary descriptors. The classification system is described below, and the classification codes are summarized in Table 2. In Table 3, we apply these codes to the objects from our survey, and in Table 4, to previously imaged PPNs.

First, we divide the observed primary morphologies into four major classes: bipolar (B), multipolar (M), elongated (E), and irregular (I). There is no class referring to round shapes, because we have not found any object in which the central post-AGB structure appears round. The "bipolar," or B, shape is defined by objects which show two primary, diametrically opposed lobes, centered
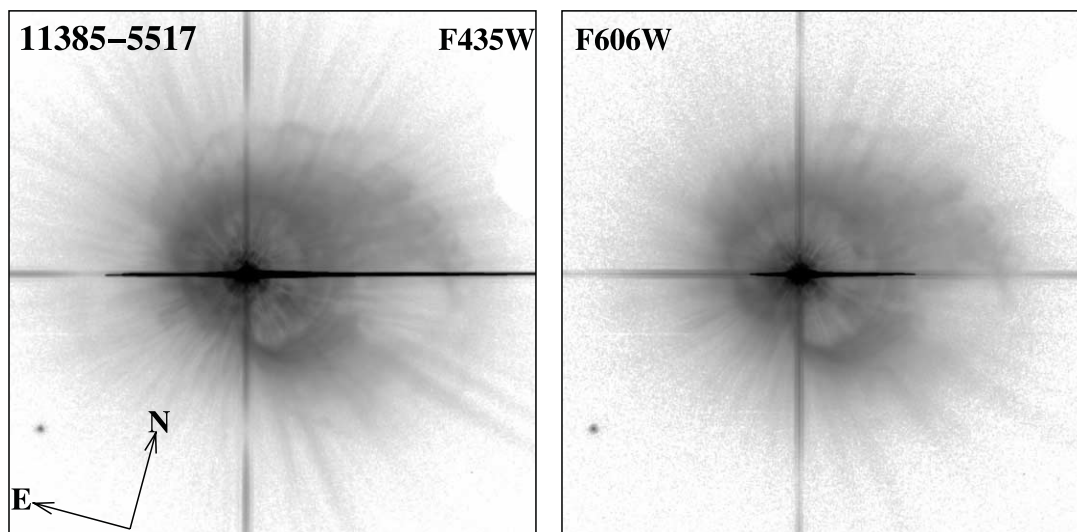
Fig. 1.—*HST* image (log stretch) of the young PPN IRAS 11385−5517 (12.5″ × 12.5″).

on the central star (or center of mass if a binary system) or its expected location (e.g., IRAS 13557−6442, Fig. 4; IRAS 15452−5459, Fig. 6). The pair of lobes must have a "pinched-in" shape in the region around the center from where they emanate, and/or the lobes should be visible on both sides of a minimum-light-intensity central region (presumably due to an obscuring dust lane; see below). The "multipolar," or M, shape is defined by objects having more than one primary lobe on either side of the center (IRAS 19024+0044, Fig. 15; IRAS 19475+3119, Fig. 19). The "elongated," or E, shape is simply one which is elongated along a specific axis, i.e., is not round (e.g., IRAS 17253−2831, Fig. 9; IRAS 18420−0512, Fig. 14). The "irregular," or I, shape is de-

fined by objects in which extended circumstellar structure can be seen but no obvious lobe or shell-like structures can be identified, and which therefore do not fit into any of the previous categories (e.g., IRAS 11385−5517, Fig. 1). As the name implies, objects in the I category usually do not display axial or point-reflection symmetry.

Secondary structural features are denoted with lowercase letters following the major class. First, we add subclassifications which are related to the lobes in the B, M, or E classes; these may be open (i.e., like a vase) or closed (i.e., having a bubble structure) at their outer ends and are denoted by "o" or "c." For sources where the morphology is not sufficiently well resolved or the images are too noisy to make the "o" or "c" determination, this subclassification is not mentioned. For multipolar (i.e., M) objects, where it is possible in principle to have some lobes which are open and some which are closed, both "o" and "c" should be used.

Some PPNs show bright, compact knots in diametrically opposed pairs, normally referred to as ansae (e.g., as in IRAS 09371+1212, the Frosty Leo Nebula; Morris & Reipurth 1990; Sahai et al. 2000a); these are denoted by "an." Sometimes minor lobes can be seen, at low or intermediate latitudes, as, e.g., in the Egg Nebula (Sahai et al. 1998a) and the Frosty Leo Nebula; these are denoted by "ml." The presence of a skirtlike structure around the primary lobes (as, e.g., in Hen 3-401; Sahai et al. 1999a) is denoted by "sk." This structure is an illuminated surface lying outside the primary bipolar lobes but with the same axis of symmetry; the skirt has a larger opening angle than the primary lobes, and while it surrounds these lobes it does not have as large a radial extent. Skirt structures are most easily discerned when the nebular axis is near the plane of the sky. But if the nebular axis is sufficiently inclined toward us, it may become difficult to distinguish between a waist with a sharp edge and a skirt. We discuss this issue in § 5.5.

If there is a dark obscuring band that cuts across the center of the nebula (i.e., a minimum in an intensity cut taken along the primary long axis of the nebula and usually described as the "waist" of the nebula), its presence is denoted by "w." The dusty waist may be due to (1) an opaque dust torus that blocks light that arises or is scattered from a central region, or (2) a disk that never allows light from the central star to emerge in directions near the equatorial plane. However, our morphological classification does not distinguish between these possibilities.
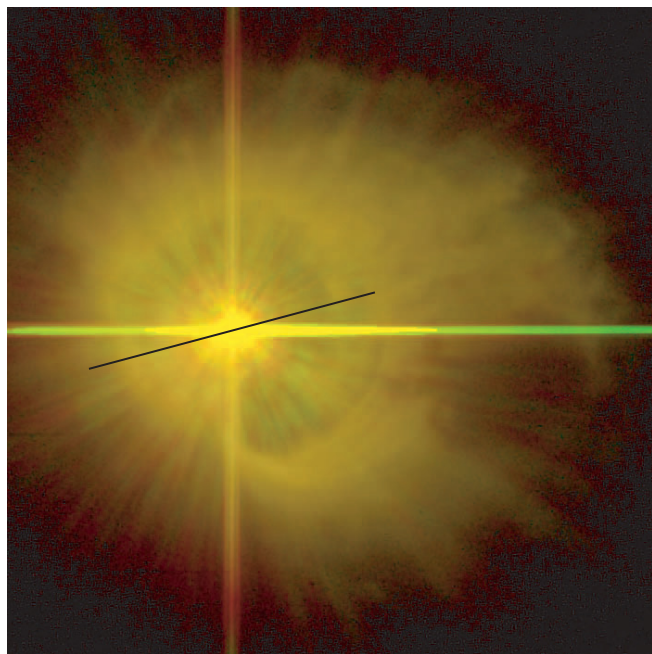

Fig. 2.—*HST* color-composite image (log stretch; *green*, F435W; *red*, F606W) of IRAS 11385−5517 (8.75″ × 8.75″). Structures due to the PSF of the bright central star are readily apparent because corresponding PSF features in the two wavelength bands occur at slightly different radial distances, whereas real circumstellar structures overlap. The vector shows the orientation (P.A. = −60°) and extent (±2″) of the high-velocity bipolar OH maser outflow.
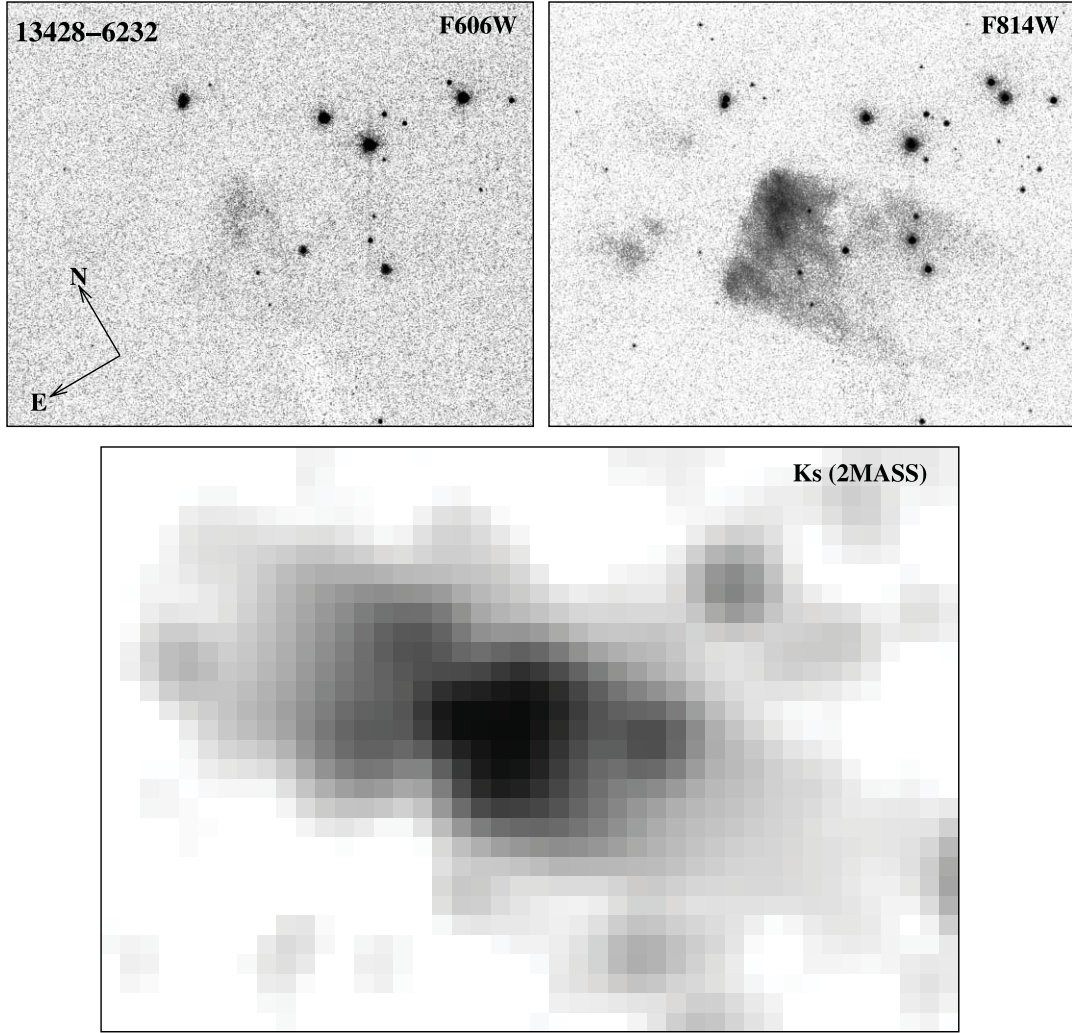
Fig. 3.— *Top*: *HST* images (log stretch) of the young PPN IRAS 13428−6232 (27.0″ × 21.75″). *Bottom*: K_s image from the 2MASS archive (44.0″ × 30.0″).
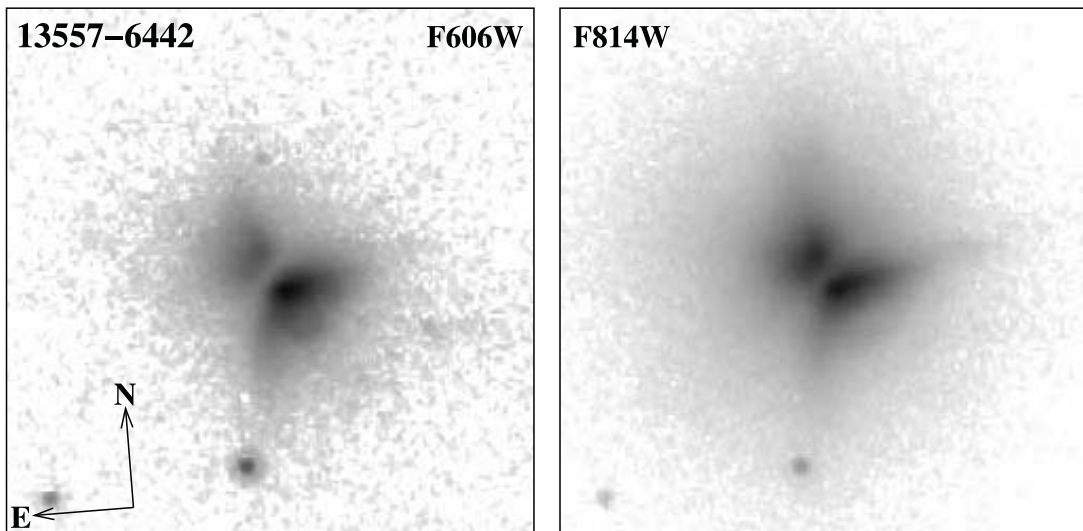

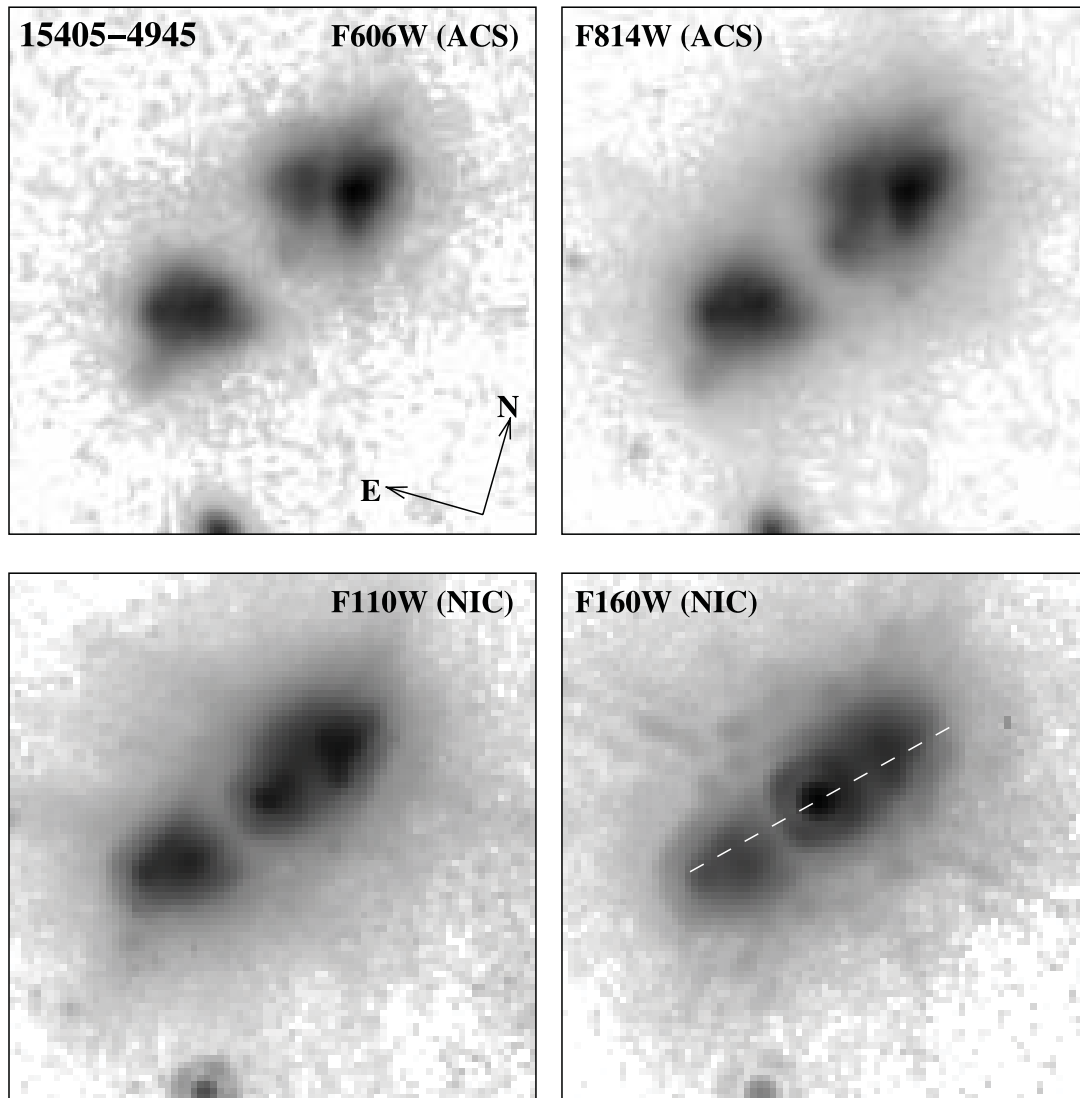Fig. 4.— *HST* images (log stretch) of the young PPN IRAS 13557−6442 (3.125″ × 3.125″).

FIG. 5.—*HST* images (log stretch) of the young PPN IRAS 15405−4945 (3.5″ × 3.5″). *Top*, ACS; *bottom*, NICMOS. The dashed white vector shown in the F160W image denotes the P.A. (−45°) and extent of the bipolar outflow seen in OH maser emission by Zijlstra et al. (2001).

For several PPNs, the waist appears to have a sharp outer (radial) edge or boundary; we denote this by adding "(b)" after "w." This outer boundary can show up in two different ways. The first, and more common, way is when the boundary is seen as a dark, convex (relative to the center of the nebula) edge cutting across one of the primary lobes.[5] A prime example of a well-studied PPN with such a "dark-edged" waist is the Egg Nebula (Sahai et al. 1998a); in our study we also find clear examples in, e.g., IRAS 19024+0044 (Fig. 15), IRAS 19292+1806 (Fig. 17), and IRAS 22036+5306 (Fig. 21). The second way is when the waist boundary smoothly transitions from a dark feature seen against the bright lobes to a brightness feature seen against the sky (or faint nebular) background in equatorial regions on either side of the lobes. The best examples of this phenomenon are provided by IRAS 17106−3046 (Kwok et al. 2000) and IRAS 04296+3429 (Sahai 1999; but see Oppenheimer et al. 2005 for a different interpretation).

If the central star can be observed (in any of the optical or near-infrared filters used with *HST* for imaging PPNs), we add the symbol ⋆, followed by a reference wavelength in parenthe-

ses. The latter is defined as the central wavelength (in microns) of the filter used for the shortest wavelength image in which the central star of the PPN can be seen. The reference wavelength helps to provide a rough qualitative comparison between the obscuring optical depths among different PPNs, where the central star is seen, since the optical depth of the dust in front the star increases toward shorter wavelengths.

Next, if there is evidence for point symmetry in the nebular structure, we denote it by "ps." This classification is not applied to axially symmetric objects, even though axial symmetry is a special case of point symmetry. The point symmetry can be of three general types: (1) the presence of two or more pairs of diametrically opposed lobes, denoted as "m" (e.g., IRAS 19475+3119, Fig. 19), (2) the ansae are distributed point-symmetrically about the center (e.g., as in Frosty Leo), denoted as "an," and (3) the overall geometric shape of the lobes is point symmetric (e.g., Hen 3-1475), denoted as "s." These three types of point symmetry are listed in parentheses after the "ps" symbol; e.g., "ps(m)" means a nebula which is point symmetric by virtue of having two or more pairs of diametrically opposed lobes. An object may possess more than one type of point symmetry; e.g., IRAS 19024+0044's point symmetry would be represented as "ps(m,an)," since it shows

---

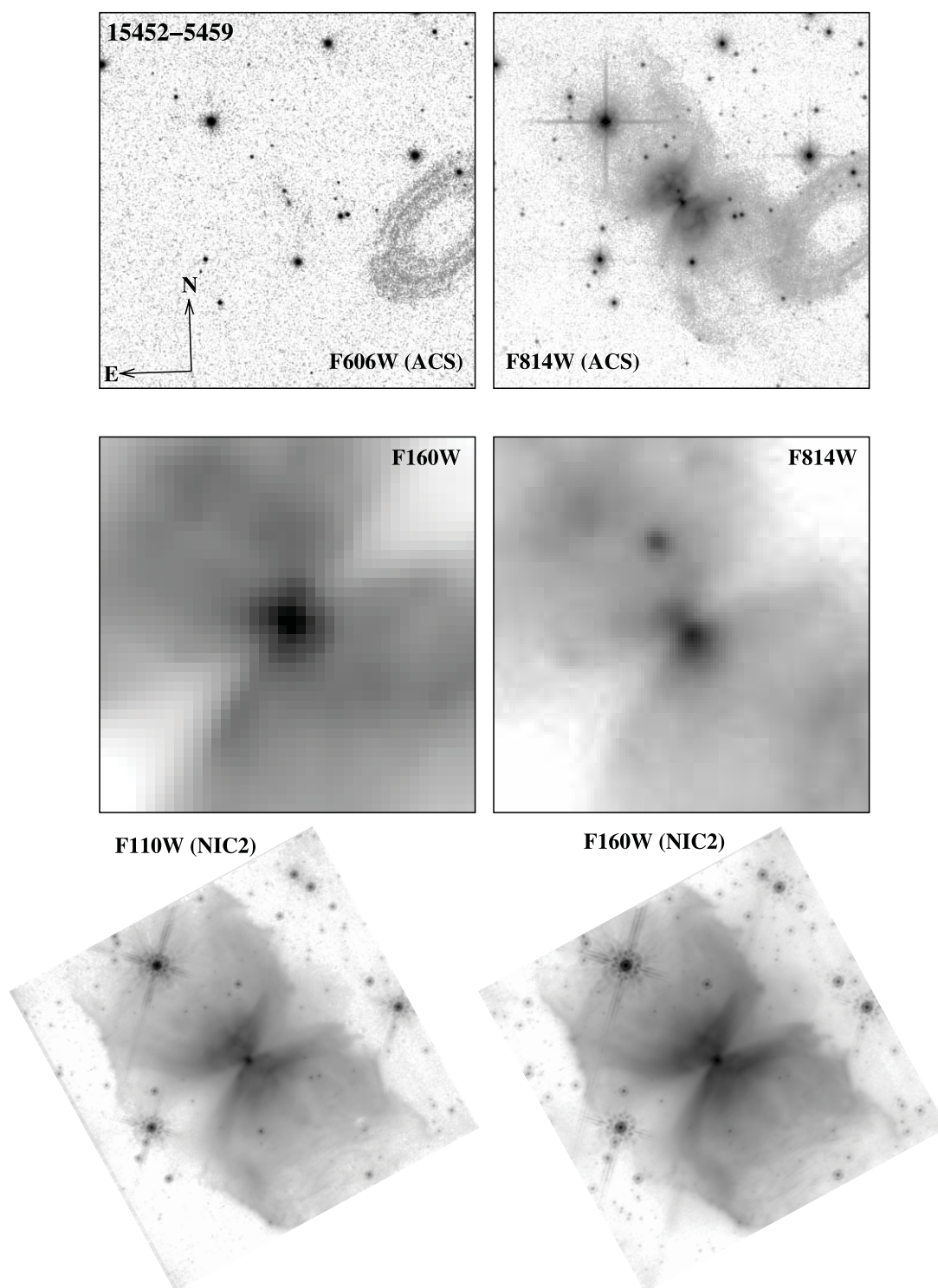[5] A detailed discussion of this issue is given in § 5.5.

F_{IG}. 6.—*HST* images (log stretch) of the young PPN IRAS 15452−5459. *Top*: Extended nebula (25.0″ × 25.0″) imaged with ACS (the elliptical shape on the right-hand edge of the image is an instrumental artifact). *Bottom*: Extended nebula (19.3″ × 19.3″) imaged with NICMOS. *Middle*: Central region (3.0″ × 3.0″).

both the presence of pairs of diametrically opposed lobes and ansae in one of the lobe pairs which are point symmetric (Sahai et al. 2005).

The presence of a halo is denoted with "h," and an "(e)" is added after it if it has a nonround, or elongated, shape. If the halo shape cannot be determined reasonably (e.g., if the halo is rather tenuous and the source lies in a field with bright nearby stars, as in the case of IRAS 17543−3102), we add "(i)," meaning that the shape is indeterminate. Thus, the default halo shape is assumed to

be round. The presence of arclike structures in the halo, as, for example, seen in the Egg Nebula (Sahai et al. 1998b), is denoted by "(a)." Note that a halo may have a smaller visible radial extent than the nebular lobes in the images shown. However, this does not necessarily imply that the physical radius to which the halo can be detected is smaller than the lobes; it is a result of the more rapid radial decrease of the halo surface brightness compared to the lobes. With azimuthal averaging, the halo can be traced to radii beyond the radial extents of the lobes.
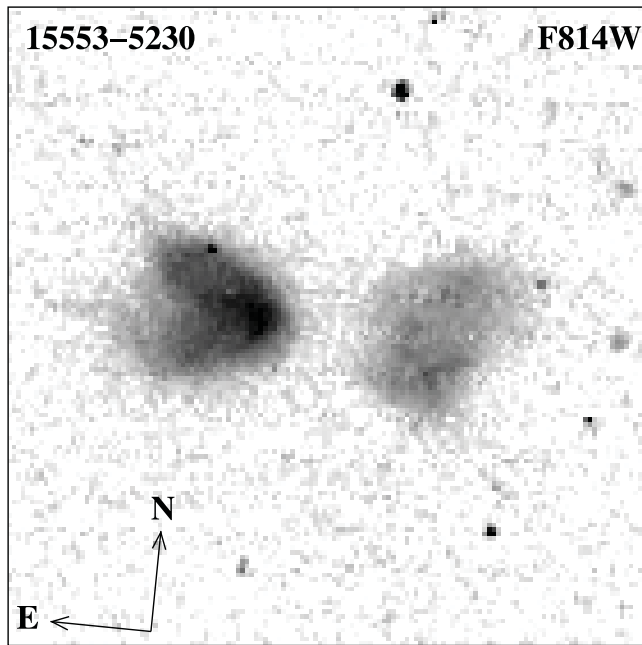
Fig. 7.—*HST* image (log stretch) of the young PPN IRAS 15553−5230 (3.5″ × 3.5″).

In a few bipolar PPNs, searchlight beams which appear to emanate from the center can be seen illuminating parts of the halo at high latitudes around the polar axis. Although the best example of this phenomenon is provided by the Egg Nebula (Sahai et al. 1998b), similar features have been seen in four other PPNs: IRAS 20028+3910 (Hrivnak et al. 2001), IRAS 17150−3224 (Su et al. 2003), IRAS 17245−3951 (Hrivnak et al. 1999), and IRAS 18276−1431.[6]

Note that in our system, the M, or multipolar, classification does not necessarily imply the point-symmetric subclass, denoted by "m," even though for the two M objects in our survey, IRAS 19024+0044 and IRAS 19475+3119, the lobes appear in dia-

---

[6] IRAS 18276 is included in our survey; a detailed study of this object utilizing the *HST* images shown here and other data has been presented by Sánchez Contreras et al. (2007).

metrically opposed (i.e., point-symmetric) pairs. The reason for this is that it may be possible for objects to have multiple lobes, all of which cannot be unambiguously grouped into diametrically opposed pairs. Specific examples of such objects are the Starfish Twins (He 2-47 and M1-37), two young PNs with multiple lobes described by Sahai (2000).

Similarly, the B, or bipolar, classification does not necessarily imply "w" (i.e., the presence of a dusty waist), even though most B objects have dusty waists. Specific examples of objects which are bipolar but do not show dusty waists in their images are IRAS 17440−3310 (Fig. 11) and IRAS 19306+1407 (Fig. 18). It is possible that these objects do have a dusty waist, but the waist is sufficiently tilted away from an edge-on orientation, and hence does not appear as an intensity minimum between the two lobes.

We have applied the above system to some of the most well-resolved and best-studied PPNs to ensure that it captures the important morphological characteristics of these objects. Thus, the Egg Nebula has the classification Bcw(b),ml,h(e,a,sb); Frosty Leo is Bcw(b)⋆(0.60),an,ml,ps(m,an,s); Minkowski's Footprint, M1-92 (e.g., Bujarrabal et al. 1998), is Bcw(b)⋆(0.55),an; and Hen 3-401 is Bow⋆(0.60),sk (Sahai et al. 1999a). The water-fountain PPN, IRAS 16342−3814 (Sahai et al. 1999b), is classified as Bcw,ps(s).

3.2. *Distances, Sizes, Ages, and Dust Masses*

We have estimated the distances to our survey sources (D_L) assuming a fixed luminosity of 6000 $L_\odot$ for each object, rather than using kinematic distances determined from radial velocities, because these objects can quite often have large and peculiar motions relative to the general Galactic rotation. Both of the above choices have been motivated by a VLBA proper-motion study of the young PPN IRAS 19134+2131. For this object, Imai et al. (2007) determine a trigonometric parallax distance of 8 ± 0.8 kpc, giving a luminosity of 5500 $L_\odot$ and a Galactic rotation velocity of ∼125 km s^{-1}, much slower than that given by the Galactic rotation curve at IRAS 19134+2131's location. Our choice of a fixed luminosity in our computations is not meant to imply that all PPNs have this same value of luminosity, but simply to provide a convenient normalization factor for the ages and masses. The values of these parameters can then be conveniently scaled in future studies when better distance determinations of individual objects become available.
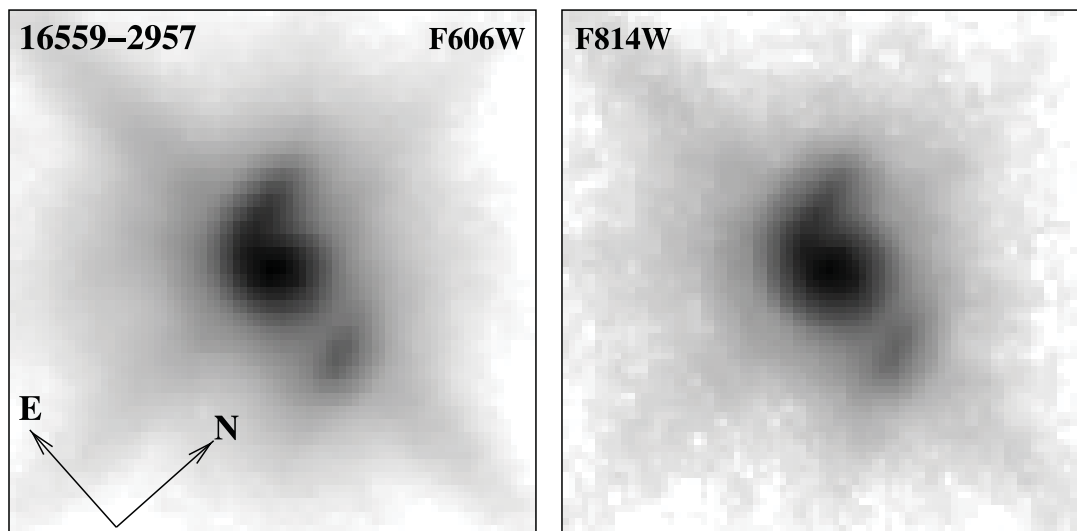

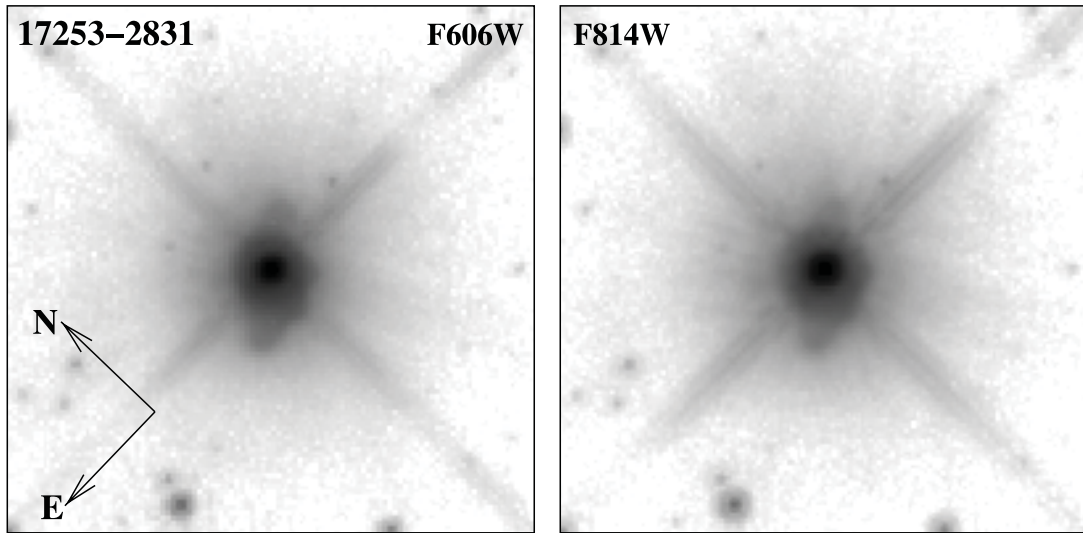Fig. 8.—*HST* images (log stretch) of the young PPN IRAS 16559−2957 (1.82″ × 1.82″).

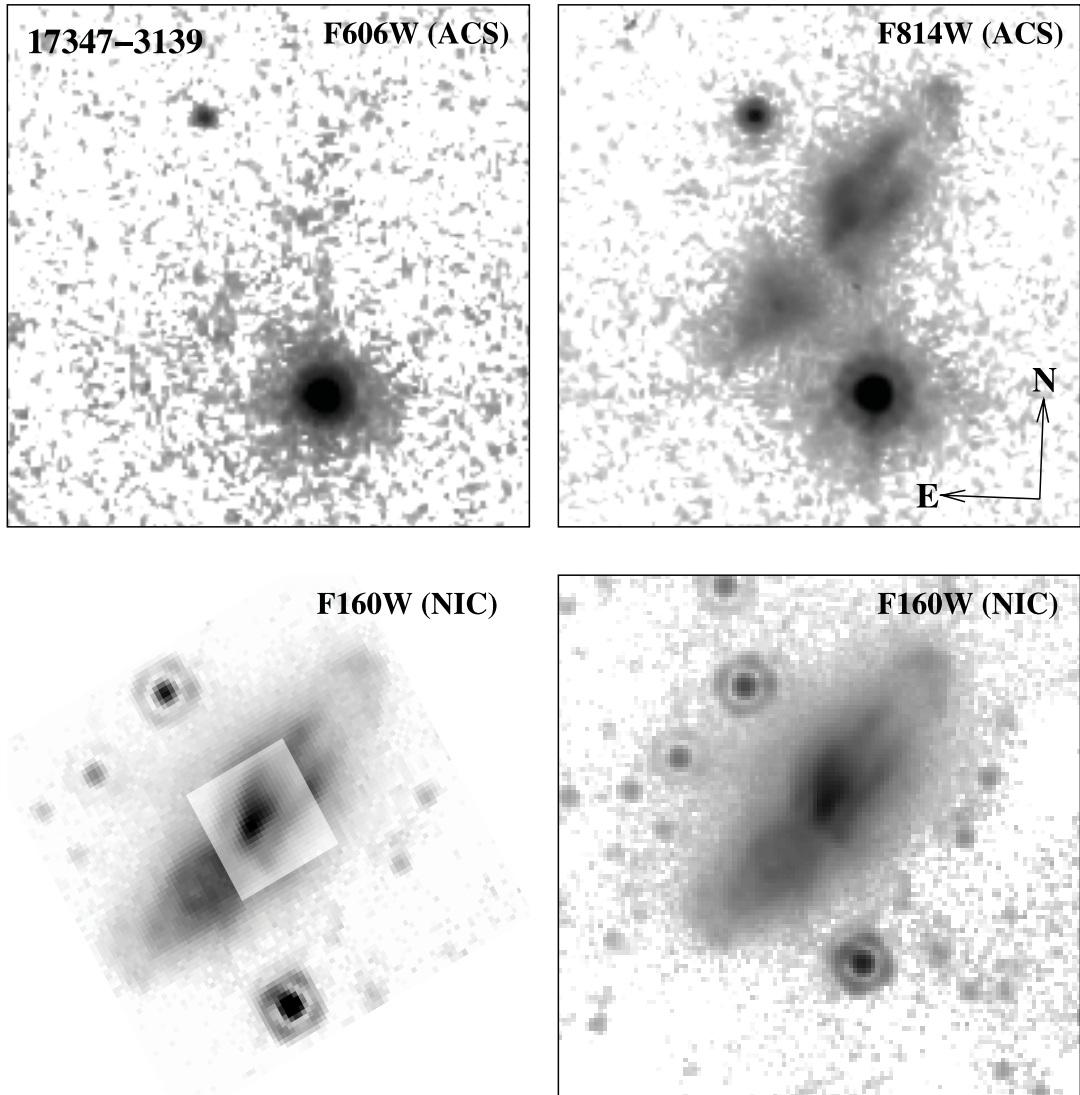FIG. 9.—*HST* images (log stretch) of the young PPN IRAS 17253−2831 (4.57″ × 4.57″).

FIG. 10.—*HST* images of the young PPN IRAS 17347−3139 (5.0″ × 5.0″). *Top panels*: ACS images using a log stretch. *Bottom panels*: NICMOS (NIC1) images. The bottom right panel shows the F160W image using a log stretch; the bottom left panel shows the same image using a linear stretch, with the intensity reduced by a factor of 5 in a central 0.85″ × 0.85″ patch, in order to better display the structure within the lobe. The faint patchy structure seen to the right of and below the middle of the nebula in the F160W log-stretch image is an instrumental artifact.
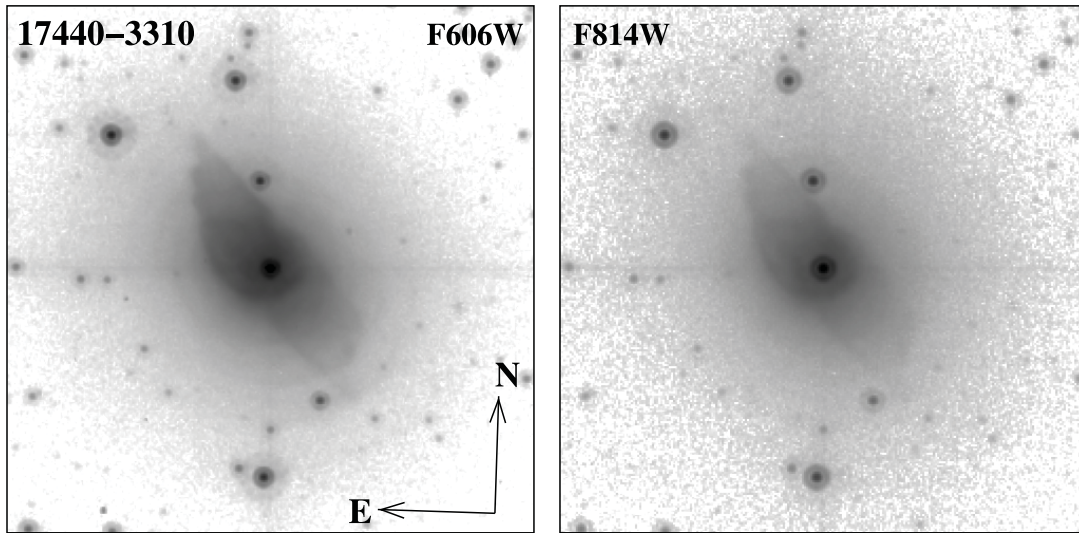
Fig. 11.—*HST* images (log stretch) of the young PPN IRAS 17440−3310 (5.0″ × 5.0″).
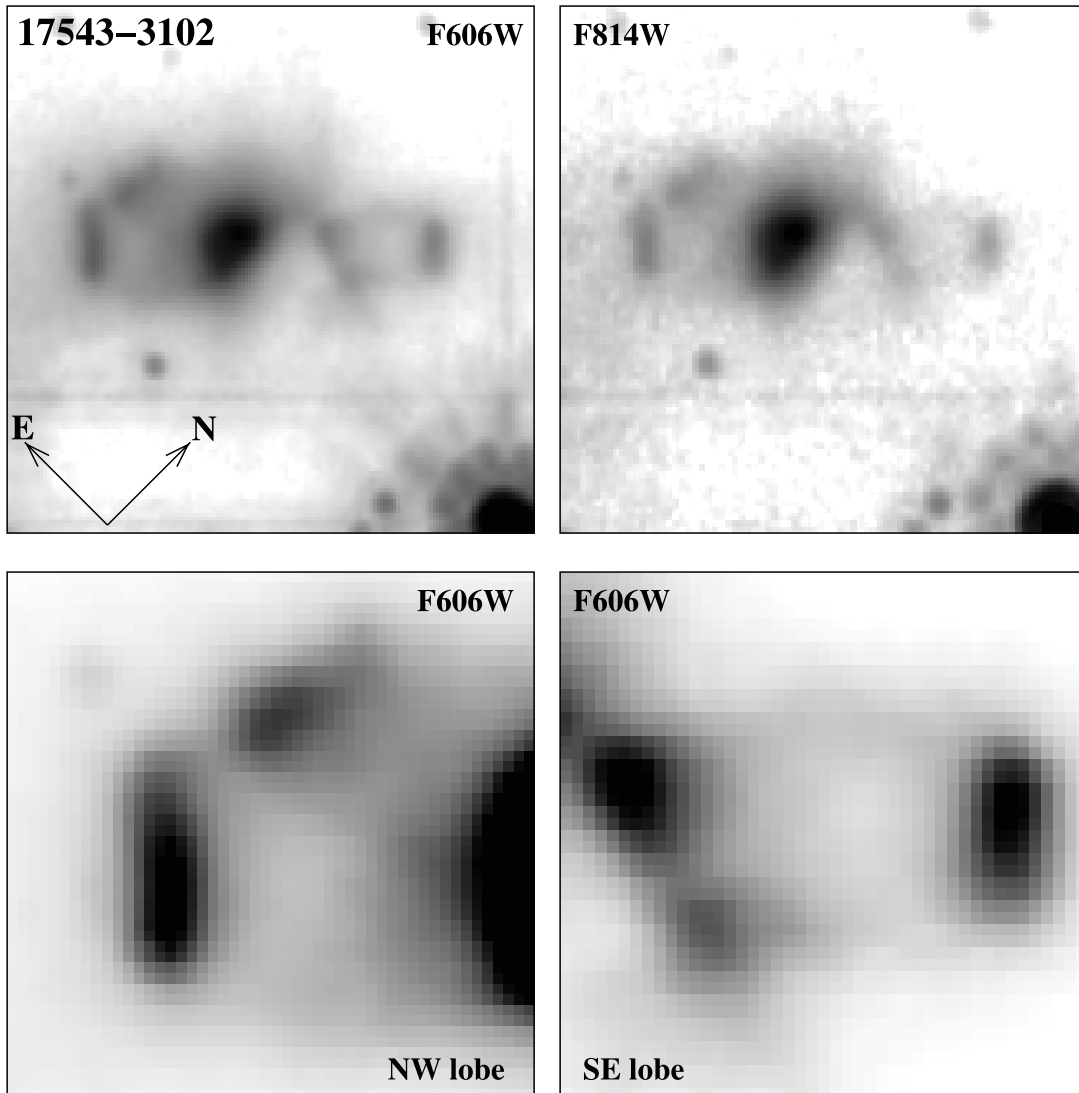
Fig. 12.—*HST* images of the young PPN IRAS 17543−3102 (2.0″ × 2.0″). *Top panels*: F606W and F814 images on a log stretch . *Bottom panels*: Magnified views (0.56″ × 0.56″) of the northwest and southeast parts of the nebula in the F606W image on a linear stretch, with the central region saturated in order to bring out the shape and structure of the lobes.
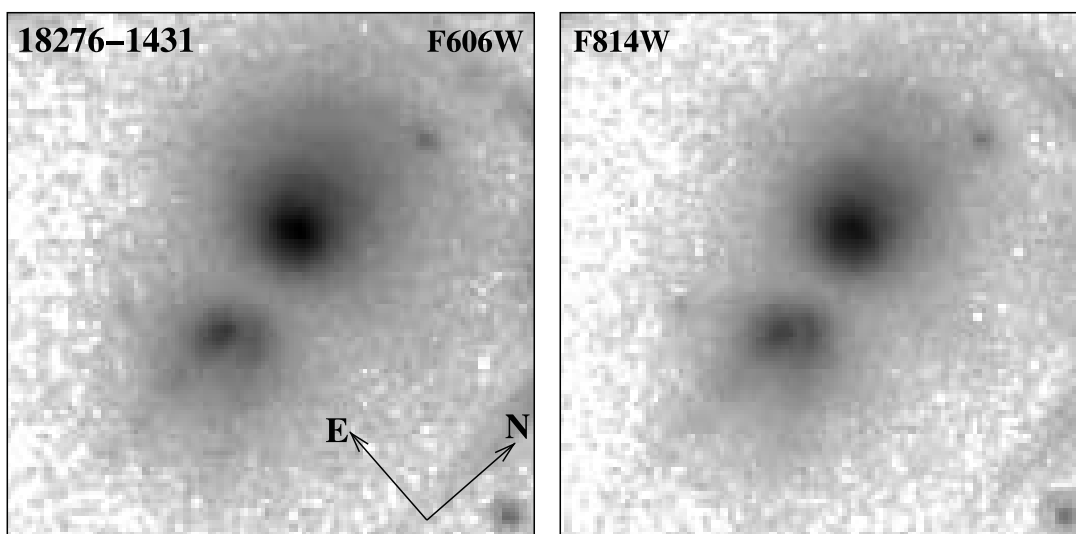
FIG. 13.—*HST* images (log stretch) of the young PPN IRAS 18276−1431 (2.96″ × 2.96″). The linear structures on the right edge of the image are diffraction spikes due to a bright field star.

The bolometric fluxes have been computed for each object by integrating the SED from the optical to far-infrared wavelengths, using published optical, *JHK*-band, *Midcourse Space Experiment* (*MSX*), and *IRAS* fluxes. For all objects where the central star is not visible, the total flux for wavelengths $\lambda \lesssim 2~\mu$m is quite small. In objects where the central star is visible, this short-wavelength flux can make a significant contribution to the bolometric flux; hence, our luminosity determination is somewhat affected by the unknown amount of interstellar extinction.

For each PPN, we have estimated the radial extent of the central aspherical structure (in arcseconds), which presumably represents the post-AGB mass loss (r_{PAGB}), and the radial extent of the halo (in arcseconds) surrounding this structure (when it is present), which presumably represents the AGB mass loss (r_{AGB}). For closed lobes, r_{PAGB} is measured radially outward from the geometric center of the nebula (or the central star, when visible) to the most distant lobe structure along the lobe axis. If the lobes are "open" at their ends, then r_{PAGB} is defined as the radial offset of the most distant point on the lobe. If several lobes are present, or if the lobes on either side of the center have different lengths,

the longest one is selected. For objects classified as I, i.e., when lobe structures are not visible, r_{PAGB} is defined as the radius to the most distant nonspherical structure. We have used azimuthal averaging to measure the radial extent of the halos.[7] The azimuthal averages are done carefully in order to avoid the angular regions which are occupied by the nebular lobes. If a halo cannot be detected, we make the reasonable assumption that $r_{AGB} = r_{PAGB}$, motivated by the fact that the lobes result from the interaction of a fast AGB wind with a surrounding AGB envelope.

A post-AGB timescale, t_{PAGB},[8] is derived by converting r_{PAGB} from angular units to linear units using the luminosity-based distances and dividing it by a nominal outflow speed of 150 km s^{-1} (which is typical of the outflow speeds derived for the lobes of individual well-studied PPNs), since individual outflow speeds

---

[7] Specifically, on a log-log plot of the averaged intensity vs. radius, the former drops smoothly out to r_{AGB}, where it reaches the background-subtracted sky level and starts showing large fluctuations (due to noise and/or the presence of many faint stars).

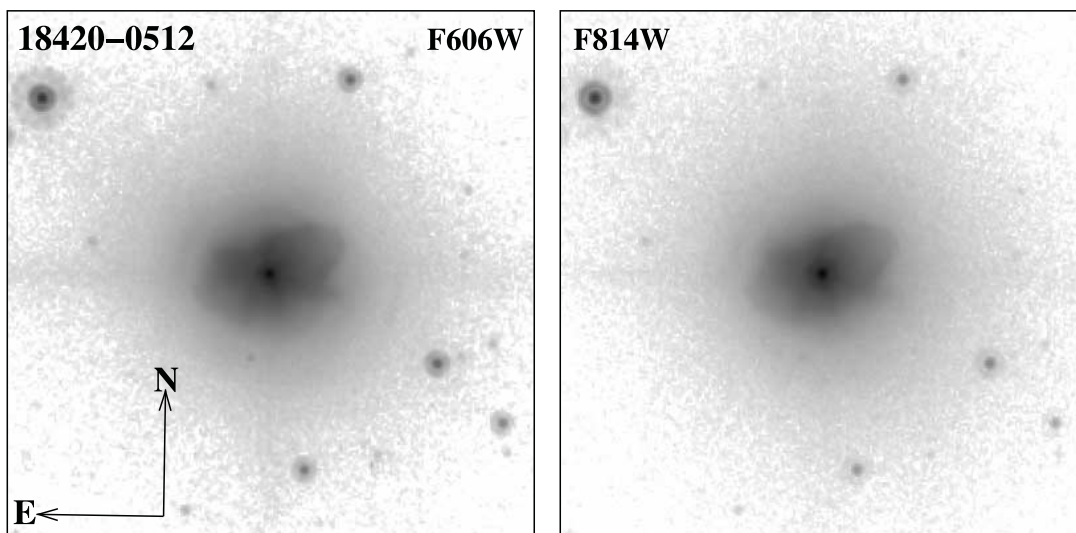[8] Rounded to the nearest 5 yr in Table 3.

FIG. 14.—*HST* images (log stretch) of the young PPN IRAS 18420−0512 (5.0″ × 5.0″).
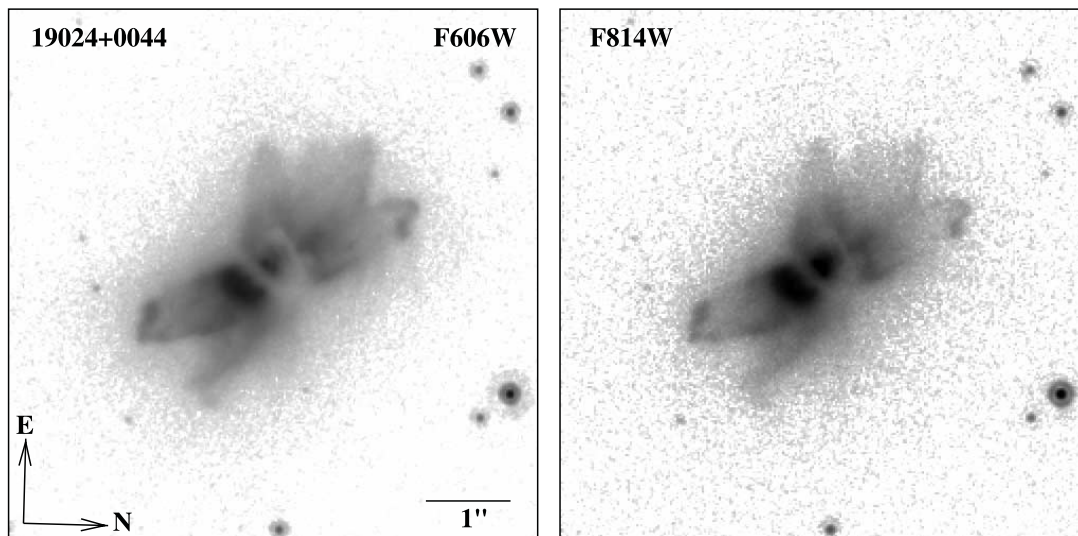
FIG. 15.—*HST* images (log stretch) of the young PPN IRAS 19024+0044 ($6.25'' \times 6.25''$).

for the material in the lobes of most objects have not been measured as yet, nor are the inclination angles of the lobe axes well known. In objects with a halo, an AGB mass-ejection timescale (t_{AGB})[9] is computed by dividing the linear radius of the halo $(r_{AGB}D_L)$ by the expansion velocity as derived from molecular line data (either OH 18 cm maser line or CO millimeter-wave line emission). Since the outer radius of the halo is most likely determined by the steadily decreasing halo surface brightness falling below the noise (due to a decrease in density, as well as central illumination), r_{AGB} and, correspondingly, t_{AGB} should be understood as lower limits. By using azimuthal averaging, we can trace the halos out to significantly larger radial distances than possible with pencil cuts of the intensity. The values of r_{AGB} given in Table 3 thus found are typically much larger than can be seen in the displayed images, where the intensity scales and stretches are chosen in order to display the central aspherical structures most clearly.

We have fitted the SED of each object from the near-infrared (K band) to the far-infrared (as defined by *MSX* and *IRAS* fluxes)

using a multicomponent model (Sahai et al. 1991). A power-law (λ^{-p}, where $p = 1.5$) dust emissivity with a value of 150 cm^2 g^{-1} (per unit *dust* mass) at 60 μm (Jura 1986) is used to fit the SED with a "cool," a "warm," and a "hot" component. The mass of the cool component, which is robustly fitted since the bulk of the emission comes from cool dust, is significantly larger than the other two components. This mass and the temperature of the cool component are therefore reported in Table 3. Comparison of the results of our simple models with those utilizing radiative transfer codes to determine the temperature distribution in detail (e.g., for IRAS 19475+3119) indicate that the simple model gives dust masses that are lower than the more accurate values by a factor of 0.6–0.8.

We have found no obvious correlations between the morphologies and the post-AGB ages, dust shell masses, or temperatures.

4. INDIVIDUAL SOURCES

IRAS 11385−5517.—This object (HD 101584) is well known for its highly collimated, high-velocity bipolar outflow seen in OH maser emission (te Lintel Hekkert et al. 1992) and massive molecular outflows (as seen in CO rotational line emission; Trams et al.

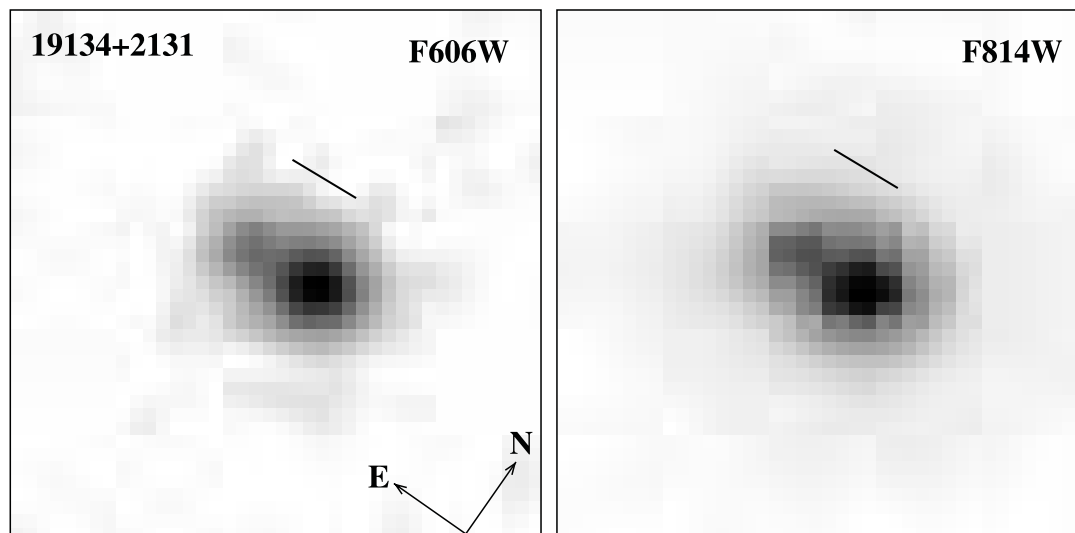[9] Rounded to the nearest 50 yr in Table 3.

FIG. 16.—*HST* images (square-root stretch) of the young PPN IRAS 19134+2131 ($1.0'' \times 1.0''$). The straight line segment shows the P.A. and separation of the blueshifted and redshifted H$_2$O maser-jet spot clusters in this object observed by Imai et al. (2007).
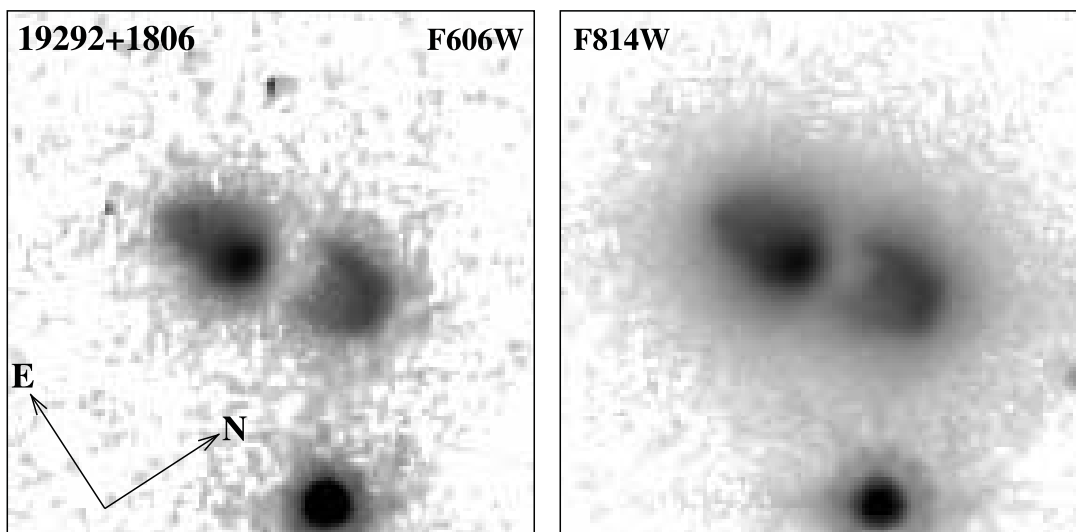
HST IMAGING SURVEY OF PPNs

Fɪɢ. 17.— *HST* images (log stretch) of the young PPN IRAS 19292+1806 (3.5″ × 3.5″).

1990). The optical morphology is irregular (Fig. 1). The central star has been classified as F0 Iape (Hoffleit et al. 1983) and A6 Ia (Sivarani et al. 1999; these authors contest Bakker et al.'s [1996] hotter, i.e., B9 II, classification) and believed to be in a close binary (Bakker et al. 1996). Although the central star is heavily saturated in both images and produces a significant PSF contribution (e.g., radial streaks), the nebular structure is easily discernible, since all features which do not change their radial distance from the center as a function of wavelength have an astrophysical origin (Fig. 2). The redshifted and blueshifted OH 1667 MHz emission features define an axis of bipolarity with P.A. $= -60°$ (te Lintel Hekkert et al. 1992).

IRAS 13428−6232.—This object appears to be rather extended, with a bright cylindrical lobe seen in the F814W image on the southwest side; the inner parts of a very faint counterpart can be seen on the northeast side (Fig. 3). The geometry is intrinsically bipolar, as can be seen in *JHK* images from the 2MASS archive and a *K*-band image by Van de Steene et al. (2000). The near-IR images show both lobes of the bipolar nebula very clearly. The cylindrical lobes are significantly more extended, as seen in the 2MASS images: e.g., the *K*-band image (Fig. 3)

shows that the brighter (southern) lobe extends to about 24.7″ along the nebular axis, compared to about 15.7″ in the *HST* F814W image. The dusty waist has a flared shape in the *K*-band image, compared to the F814W image, where its edge bordering the southwest lobe is quite straight. This change in shape is easily understood as resulting from a decrease in the disk optical depth with wavelength from 0.8 to 2 μm. The central star of the nebula is clearly visible in the *K*-band image in Van de Steene et al. (2000), which has smaller pixels (0.25″) than the 2MASS image (1.0″). The nebula is much fainter in the F606W image. Therefore, although it has been listed as a possible young PN by Preite-Martinez (1988), the lack of nebulosity in the F606W filter (which covers the Hα line) shows that any Hα emission, if present, is very weak, indicating that the circumstellar material has not been ionized substantially. In the compilation by Kwok et al. (1997), the LRS spectrum of IRAS 13428 is classified as "H," i.e., having a red continuum with either a 9.7 μm silicate absorption feature or a 11.3 μm PAH emission feature, so its chemistry is unknown.

IRAS 13557−6442.—This object is bipolar, with an hourglass shape and a dense waist seen almost edge-on (Fig. 4). The hourglass nebula is surrounded by an extended round halo. Using
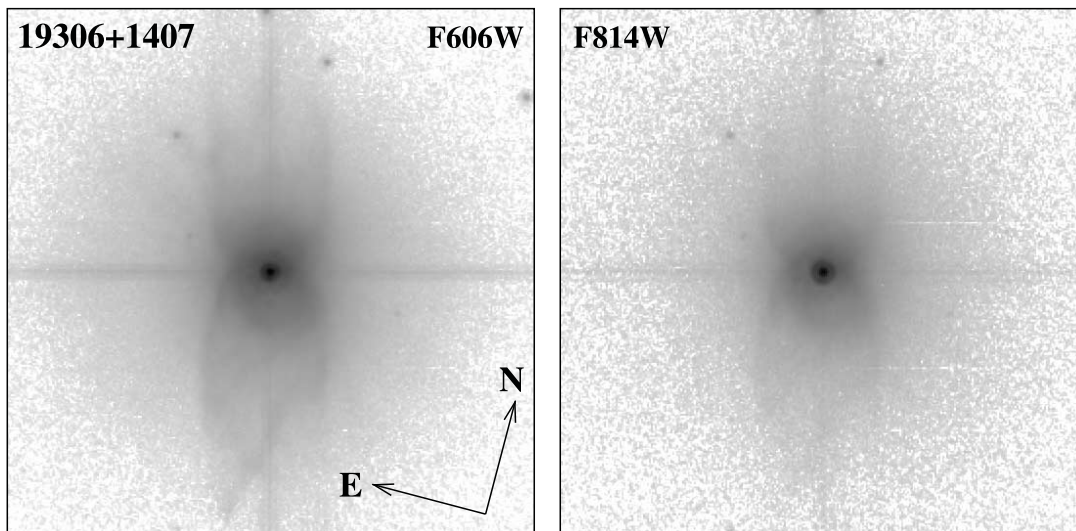

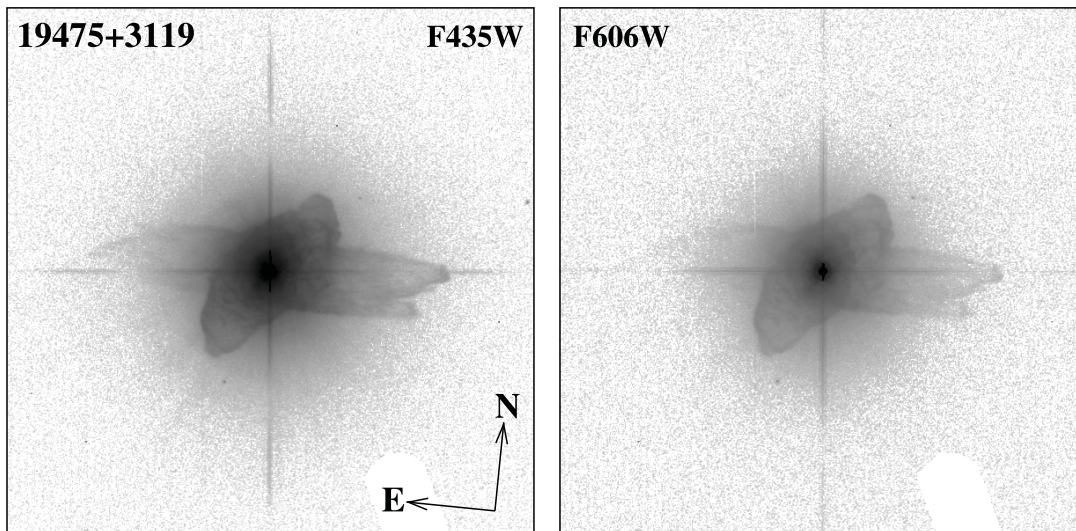Fɪɢ. 18.— *HST* images (log stretch) of the young PPN IRAS 19306+1407 (6.75″ × 6.75″).

FIG. 19.—*HST* images (log stretch) of the young PPN IRAS 19475+3119 (15.0″ × 15.0″).

azimuthal averaging, we can trace the halo out to a radius of ~3″; the radial distribution roughly follows a power law, $r^{-\beta}$, where $\beta \sim 2.3$. In this source, the MSX6C fluxes are roughly a factor of 1.7–1.5 higher in the 12–21 μm range compared to the corresponding *IRAS* fluxes (due to either variability or poor calibration). We have therefore scaled down the MSX6C fluxes by a factor of 1.6 in generating its SED. Since the blue and red peaks of the OH maser emission line are separated by only 3 km s^{-1}, it is unlikely that the standard interpretation of this separation representing twice the recent AGB CSE expansion velocity is applicable. We have therefore assumed $V_{\exp} = 15$ km s^{-1}, which gives an age of $t_{\mathrm{AGB}} = 3200(D_L/3.3\ \mathrm{kpc})$ yr for the halo.

IRAS 15405−4945.—This bipolar nebula shows complex, highly structured lobes (Fig. 5). A faint elliptical halo can be seen in the F814W image. If the halo is due to a spherical AGB mass-loss envelope, the elliptical shape indicates that the AGB envelope is being indirectly illuminated by the lobes and not by a central source, or that the light from the central source cannot get out to the larger distances at low latitudes. We also obtained NICMOS images with NIC1 in the F110W and F160W filters. Although the overall shape of the bipolar lobes in these near-IR filters is

roughly similar to that in the optical ones, there are distinct differences. The central star is visible in the NIC1 images, lying midway on the line joining the tips of the lobes. The OH masers in this object span a very large range (80 km s^{-1} in the 1612 MHz line, 105 km s^{-1} in the 1665 MHz line, and 155 km s^{-1} in the 1667 MHz line) and lie along a P.A. of −45°, covering an elongated region with a major axis of ~2″ (Zijlstra et al. 2001). Thus, the extent of the fast outflow as traced by the OH masers matches the size of the bipolar nebula seen in the *HST* images. We estimate an expansion velocity of the AGB envelope of 13.5 km s^{-1} from the separation of the prominent peaks in the OH 1665 MHz line profile; and, given the 3″ extent of the halo, we find $t_{\mathrm{AGB}} = 5200(D_L/4.9\ \mathrm{kpc})$ yr.

IRAS 15452−5459.—This object shows a very extended hourglass-shaped nebula in the F814W image; almost no nebulosity is visible in the F606W image. The two lobes are of roughly equal brightness and are separated by a flared, edge-on waist (Fig. 6). We also obtained NICMOS images with NIC2 in the F110W, F160W, and F205W filters; the shape of the extended nebula appears quite similar in all three near-IR filters compared to that in the F814W filter. However, the central star, which is not
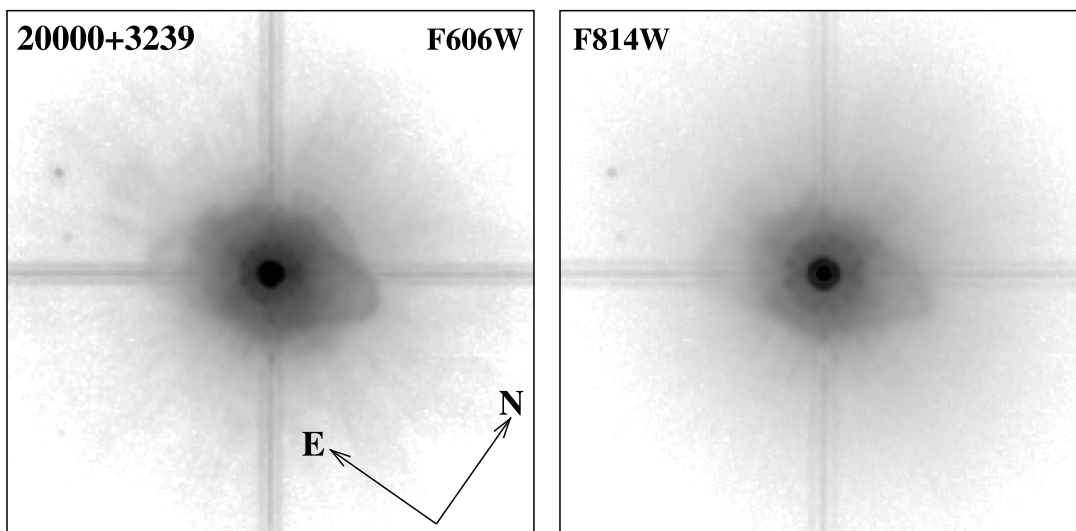

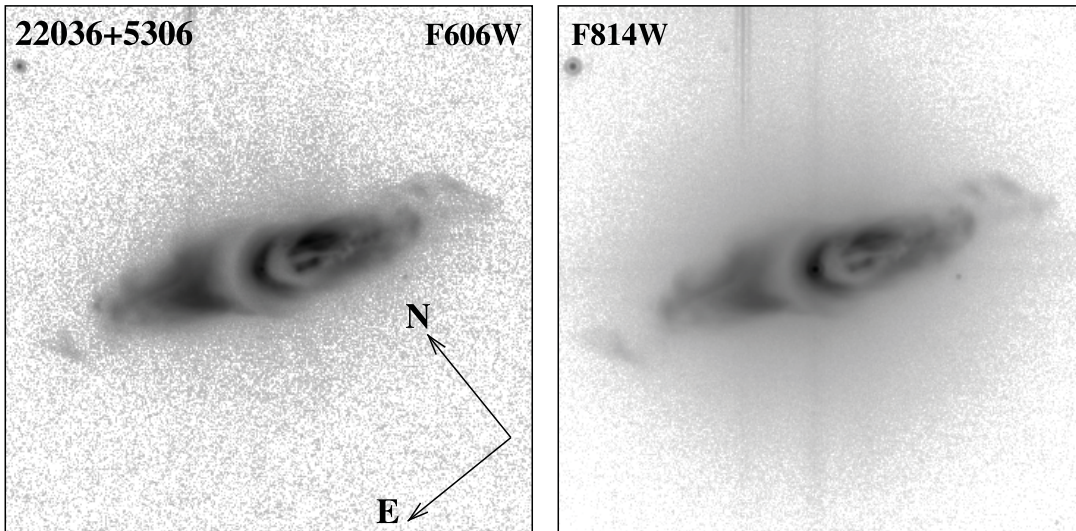FIG. 20.—*HST* images (log stretch) of the young PPN IRAS 20000+3239 (5.0″ × 5.0″).

Fig. 21.—*HST* images (log stretch) of the young PPN IRAS 22036+5306 (9.0″ × 9.0″). The vertical stripes are optical artifacts.

visible in the F814W image, appears visible at the geometric center of the dust lane in the near-IR images. The waist, which appears as a minimum in intensity between the bright inner regions of the bipolar lobes, appears as a bright feature against the sky background beyond the western lateral periphery of the lobes and shows a distinct, curved outer edge. The OH maser emission in this object shows blue and red peaks at -67.2 and -48.3 km s^{-1}, implying an outflow speed of 9.5 km s^{-1}. Since a halo is not observed directly, we have assumed $r_{AGB} = r_{PAGB}$ to compute an estimated AGB mass-loss timescale, $t_{AGB} = 9850(D_L/1.7$ kpc) yr.

IRAS 15553−5230.—This object is bipolar, with an hourglass shape and a dense waist seen almost edge-on (Fig. 7), very similar to IRAS 13557. It was only imaged in F814W. No halo can be seen. No line emission (either CO or OH) has been detected from the object, and the AGB expansion velocity is unknown. Assuming a typical AGB outflow velocity of $V_{exp} = 15$ km s^{-1}, we find $t_{AGB} = 1430(D_L/4.3$ kpc) yr. We do not know if IRAS 15553 is oxygen- or carbon-rich; although it is included in the compilation by Kwok et al. (1997), its LRS spectrum is classified as "H," i.e., having a red continuum with either a 9.7 μm silicate absorption feature or a 11.3 μm PAH emission feature.

IRAS 16559−2957.—This object (with an F5 Iab:e central star; SIMBAD database) shows a compact nebula with filamentary structures on either side of a central, round core (Fig. 8). The eastern filament emanates from the central core, whereas the western one is separated from the latter by a dark band, which most likely represents a tilted, dusty equatorial structure. Using azimuthal averaging, we can trace a tenuous halo out to a radius of about 3.5″. The radial distribution follows a power law, $r^{-\beta}$, where $\beta \sim 2.8$. Using an AGB envelope expansion velocity of 14.8 km s^{-1} derived from OH maser data, we find that the AGB envelope was characterized by a roughly constant mass-loss rate over a period $t_{AGB} = 5850(D_L/5.2$ kpc) yr.

IRAS 17253−2831.—This object has point-symmetrically shaped lobes and is surrounded by an extended round halo (Fig. 9). The OH maser 1612 MHz profile shows two prominent peaks at V_{LSR} velocities of -71.4 and -53.2 km s^{-1} (implying an AGB envelope expansion velocity of 9.1 km s^{-1}); the emission at velocities within these peaks is confined to a poorly resolved, roughly elliptical region of size about 0.35″ (Zijlstra et al. 2001). Using azimuthal averaging, we can trace the halo out to a radius of $\sim$2.7″; the radial distribution follows a power law, $r^{-\beta}$, where
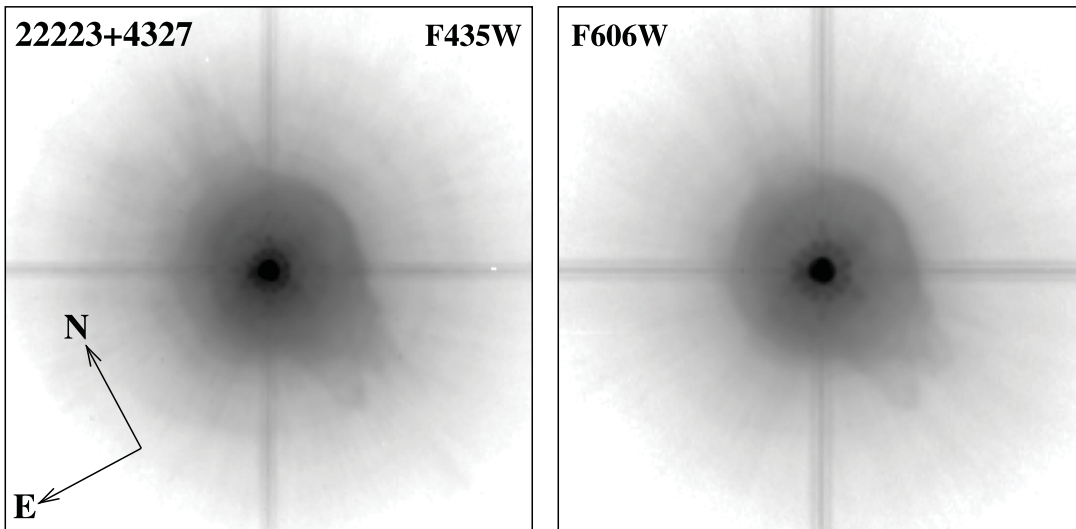
Fig. 22.—*HST* images (log stretch) of the young PPN IRAS 22223+4327 (5.0″ × 5.0″).
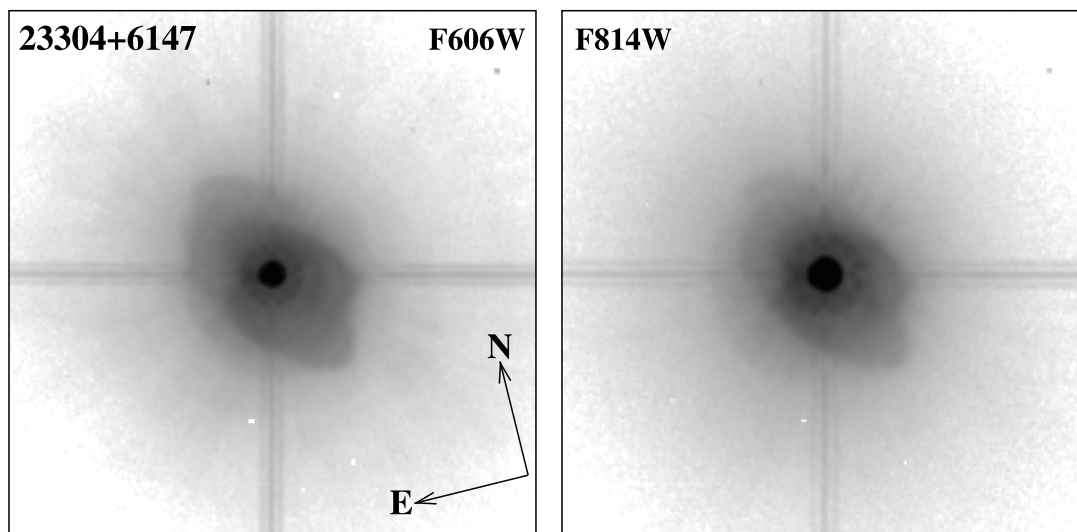
FIG. 23.—*HST* images (log stretch) of the young PPN IRAS 23304+6147 (5.0″ × 5.0″).

$\beta \sim 2.9$, signifying a roughly constant mass-loss rate over a period $t_{AGB} = 10,800(D_L/7.7 \text{ kpc})$ yr. Zijlstra et al. (2001) believe that there is a fast bipolar outflow based on the locations of maser features at velocities outside the main profile peaks, but do not provide a position angle which can be compared with that of the optical nebula in our *HST* images.

IRAS 17347−3139.—The F814W image shows a bipolar nebula with collimated lobes separated by a dense waist; almost no nebulosity is visible in the F606W image. The lobes show significant differences from each other in their structure (Fig. 10). We also obtained NICMOS images with NIC1 in the F110W (not shown) and F160W filters (Fig. 10). The shape of the extended nebula appears quite similar in both near-IR filters compared to that in the F814W filter. The two lobes are rather asymmetric in shape and size, with the northwest lobe being significantly longer in extent. The latter also shows a very bright, collimated feature in its innermost region (Fig. 10, *bottom left*) located midway between the lateral boundaries of the lobe. This collimated feature opens into a Y-shape; the right-hand fork of this Y-structure is significantly longer that the left-hand one and extends along the body of the lobe on a curved trajectory which, when extrapolated, culminates at the bright, bow-shaped tip of this lobe. These collimated structures are indicative of the presence of a highly collimated jet whose axis has precessed while it has sculpted out the northwest lobe. A faint elliptical halo can be seen around the lobes in the F160W image. Using azimuthal averaging, we can trace this halo out to a radius of $\sim 2''$. Although OH maser emission is detected, the line profile is weak and complex (Zijlstra et al. 1989) and does not allow us to determine an AGB expansion velocity. Therefore, assuming a typical AGB outflow velocity of $V_{exp} = 15 \text{ km s}^{-1}$, we find $t_{AGB} = 1950(D_L/3.1 \text{ kpc})$ yr.

The detection of radio continuum from this object (de Gregorio-Monsalvo et al. 2004) suggests that IRAS 17347−3139 may be approaching the young PN phase, or may already have become a very young PN (note that two other well-known PPNs, M1-92 and AFGL 618, also show radio continuum emission). De Gregorio-Monsalvo et al. also find H_2O maser emission, with a double-peaked profile having a total width of about 9 km s^{-1}, which they associate with a central toroid.

IRAS 17440−3310.—This object has point-symmetric lobes and is surrounded by an extended round halo (Fig. 11). In the F606W image, a few circular arcs can be seen in the halo at low contrast. Using azimuthal averaging, we can trace the halo out to a radius of $\sim 4''$; the radial distribution follows a power law, $r^{-\beta}$, where $\beta \sim 3$. Using an AGB envelope expansion velocity of 14.6 km s^{-1} derived from OH maser data, we find that the AGB envelope was characterized by a roughly constant mass-loss rate over a period of $t_{AGB} = 9850(D_L/7.6 \text{ kpc})$ yr.

IRAS 17543−3102.—This object shows a complex shape, with a central bright nebulous region and two ansae located along a southeast-northwest axis. The bright region is located closer to the southeast ansa. Each of the ansae are aligned tangentially to the long axis of the nebula, defined by the vector joining the midpoints of the ansae (Fig. 12). A linear stretch of the F606W image, with the central region saturated to bring out faint structures, shows that the ansae define the ends of elongated, lobelike structures. Two additional bright, knotty structures can be seen, one located northeast of the southeast ansa and another located northwest of the central region but closer to the center than the northwest ansa. Using azimuthal averaging, a faint halo can be traced out to a radius of $\sim 2''$. Because of the presence of a large number of stars in the vicinity of this object, including two rather bright ones within 1.3″ and 1.8″ of the center of the nebula, we cannot check whether or not the halo is round. The radial distribution follows a power law, $r^{-\beta}$, where $\beta \sim 2$. The AGB expansion velocity is unknown, since the OH maser emission line from this object shows a single peak. Therefore, assuming a typical AGB outflow velocity of $V_{exp} = 15 \text{ km s}^{-1}$, we find $t_{AGB} = 4600(D_L/7.3 \text{ kpc})$ yr.

IRAS 18276−1431.—This object (with a K2/K3 spectral type central star; SIMBAD database) has a bipolar shape with a central dense, roughly edge-on waist (Fig. 13) and an extended halo. The two lobes shows different shapes, and a pair of "searchlight beams" emanate from the fainter one. If the halo is due to a spherical AGB mass-loss envelope, the elliptical shape indicates that the AGB envelope is being indirectly illuminated by the lobes and not by a central source, or that the light from the central source cannot get out to the larger distances at low latitudes. A detailed study of this object, including near-infrared imaging using adaptive optics from the ground, has been presented by Sánchez Contreras et al. (2007), and we have used their results in Table 3, scaled appropriately for the small difference in distance values (3 kpc in this paper, 2.7 kpc in theirs). IRAS 18276 shows OH maser emission and is therefore O-rich.

F814W

Fig. 25.—Expanded view of the central region ($0.75'' \times 0.75''$) of the nPPN IRAS 01037+1219 (linear stretch). The orientation is the same as in Fig. 24.

(2005), we briefly summarize the main characteristics here. The object shows at least six elongated lobes, two with limb-brightened point-symmetric ansae at their tips, and a faint round halo characterized with $\beta \sim 3.2$ surrounds the lobes. Since Sahai et al. (2005) assumed a radial velocity distance of 3.5 kpc resulting

F606W

N   E

0″.5

Fig. 24.—False-color *HST* images of the nPPN IRAS 01037+1219 (with sharp features enhanced).

IRAS 18420−0512.—This object shows a central bipolar shape embedded inside an extended halo; the central star is visible (Fig. 14). One, possibly two, secondary lobes with collimated shapes emanate from the central region. Faint, roughly circular arcs can be seen in the halo. The red and blue maser peaks in the OH line profile are located at 116.0 and 93.1 km s^{-1}, giving an expansion velocity of 12.4 km s^{-1}. Using azimuthal averaging, the halo can be traced out to a radius of $\sim 3''$; the radial distribution follows a power law, $r^{-\beta}$, where $\beta \sim 3$, signifying that the AGB envelope was characterized by a roughly constant mass-loss rate over a period of $t_{\mathrm{AGB}} = 7600(D_L/6.6 \text{ kpc})$ yr.

IRAS 19024+0044.—Since a detailed multiwavelength study of this object, which has a multipolar morphology (Fig. 15) and an early-G type central star, has been reported by Sahai et al.

17047−5650   F435W

N

E

Fig. 26.—*HST* image (log stretch) of the young PPN IRAS 17047−5650 ($10.38'' \times 13.38''$).

FIG. 27.—*HST* image (log stretch) of the young PPN IRAS 21282+5050 (12.5″ × 12.5″).

FIG. 28.—*HST* image (log stretch) of the young PPN IRAS 22568+6141 (6.88″ × 9.0″).

FIG. 29.—*HST* image (log stretch) of the young PPN IRAS 19255+2123 (4.60″ × 7.34″).

FIG. 30.—*HST* (F606W) image of IRAS 05506+2414.

TABLE 2
MORPHOLOGICAL CLASSIFICATION CODES

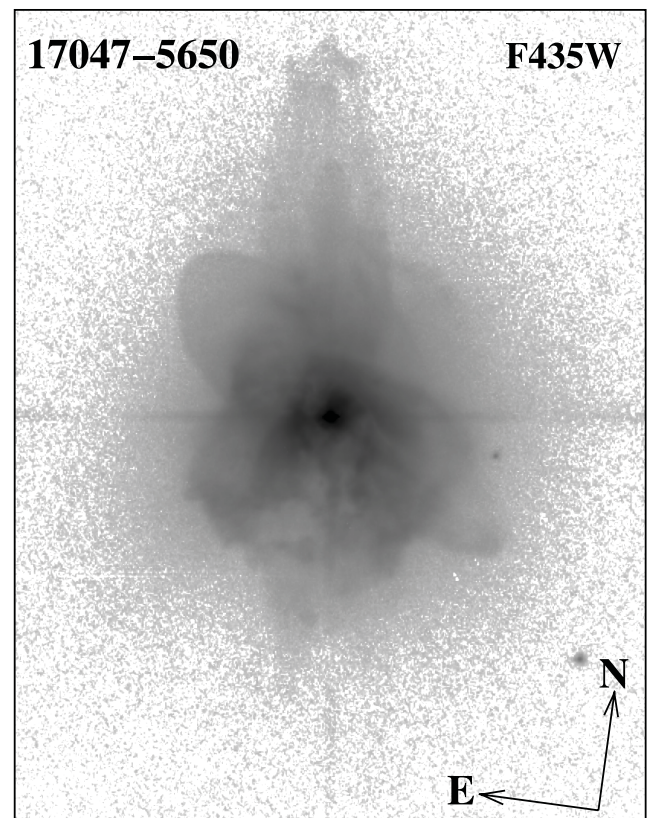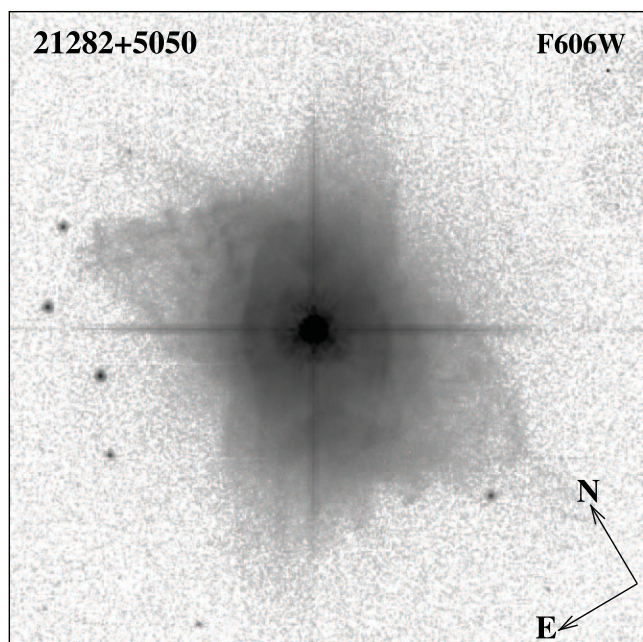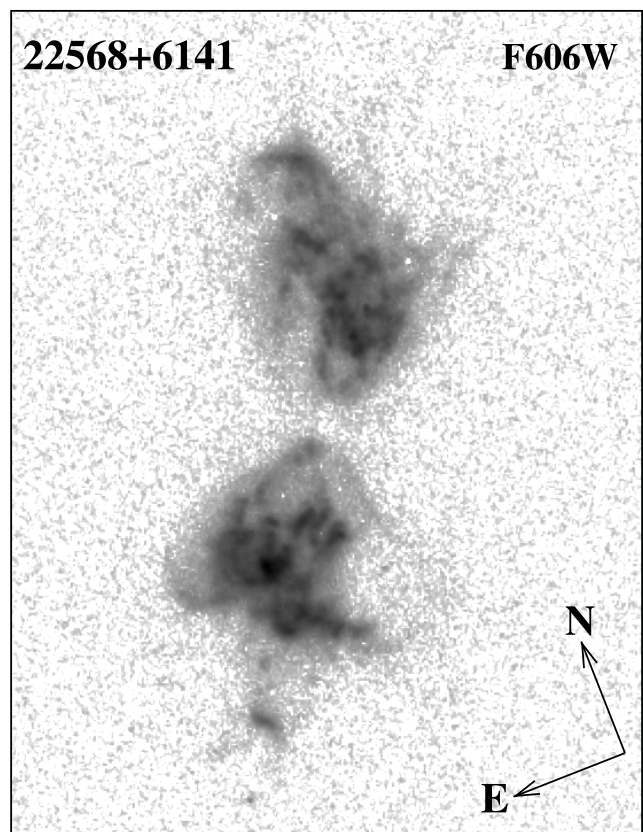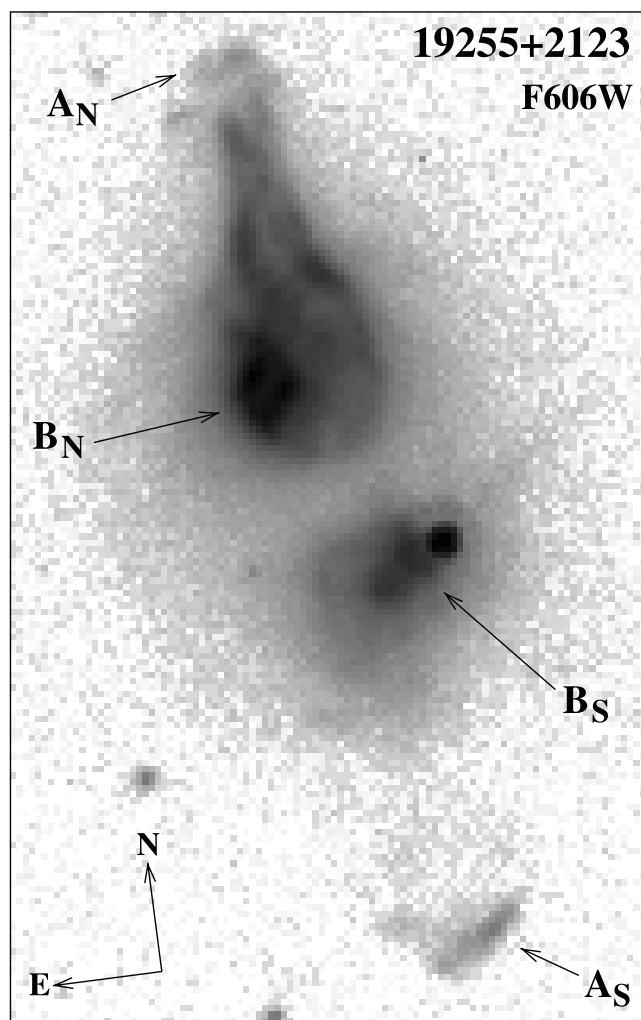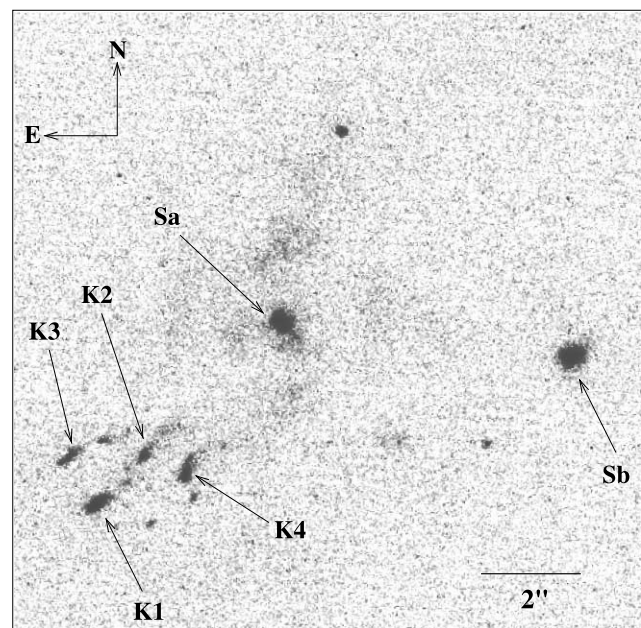| Code	Meaning
Primary Classification: Nebular Shape	
B..	Bipolar
M..	Multipolar
E..	Elongated
I...	Irregular
Secondary Classifications	
Lobe shape	
o..	Lobes open at ends
c..	Lobes closed at ends
Obscuring waist	
w..	Central obscuring waist
w(b)...	Obscuring waist has sharp radial boundary
Central star	
⋆(xx)...	Central star evident in optical and near-infrared images; xx is reference wavelength in microns (see § 3.1 for details)
Other nebular characteristics	
an..	Ansae present
ml...	Minor lobes present
sk..	Skirtlike structure present around primary lobes
Point symmetry	
ps(m)...	Two or more pairs of diametrically opposed lobes
ps(an)...	Diametrically opposed ansae present
ps(s)..	Overall geometric shape of lobes is point symmetric
Halo	
h...	Halo emission is present (relatively low surface brightness diffuse region around primary nebular structure)
h(e)...	Halo has elongated shape
h(i)..	Halo has indeterminate shape
h(a)...	Halo has centrosymmetric arclike features
h(sb)...	Searchlight beams are present

TABLE 3
PROPERTIES OF SURVEY PREPLANETARY NEBULAE

IRAS Name	F_{25}/F_{12}	Morphology	r_{PAGB} (arcsec)	t_{PAGB} (yr)	r_{AGB} (arcsec)	V_{exp} (km s^{-1})	t_{AGB} (yr)	T_d (K)	M_d ($10^{-3} M_\odot$)	Dist. (kpc)
01037+1219[a]............	0.83	E	...	...	35	20	5500	...	1.3	0.65
11385−5517..............	1.5	I⋆(0.43)	4.6	180	(4.6)	(15)	1800	74	1.3	1.2
13428−6232	15.4	Bow	24.7	1470	(24.7)	(15)	14700	88	2.9	1.9
13557−6442	1.9	Bow,h	0.8	85	3.0	(15)	3500	103	0.53	3.3
15405−4945	>11	B⋆(1.1)cw,ps(s),h(e)	1.0	155	3.0	13.5	5200	72	7.0	4.9
15452−5459	2.9	B⋆(1.1)ow	11.7	625	(11.7)	9.5	9850	87	1.8	1.7
15553−5230	4.9	Bow	1.1	145	(1.1)	(15)	1450	104	1.1	4.3
16559−2957	3.5	Bw,ps(s),h	0.35	60	3.5	14.8	5850	118	0.38	5.2
17253−2831	15.1	Ec⋆(0.60),ps(s),h	0.66	160	2.7	9.1	10800	98	1.5	7.7
17347−3139	5.3	Bcw,h(e)	1.9	185	2.0	(15)	1950	81	3.2	3.1
17440−3310	>5.1	Bc⋆(0.60),ps(s),h(a)	1.4	335	4	14.6	9850	79	5.5	7.6
17543−3102	7.9	Bc,an,h(i)	1.35	310	2	(15)	4600	83	3.6	7.3
18276−1431[b]............	5.8	Bcw,h(e,a,sb)	0.5	45	2.8	17.0	2300	50−105	4.75	3
18420−0512	25.9	Ec⋆(0.60),h(a)	0.8	170	3	12.4	7600	88	2.6	6.6
19024+0044	17.1	Mcw(b),an,ps(m,an),h	1.8	440	2	13.4	3700	109	1.2	5.1
19134+2131	3.1	Bcw	0.12	30	(0.12)	(15)	300	69	2.7	8.4
19292+1806	>9.6	Bcw(b),h(e)	0.9	150	2.5	14.6	4250	103	1.1	5.2
19306+1407	16.4	Bo⋆(0.60),h	3.2	500	4	14	6650	99	1.3	4.9
19475+3119[c]............	70.4	Mc⋆(0.43),ps(m,s),h	5.2	1660	6	15	8000	46−94	4.3	4.2
20000+3239	4.7	Ec⋆(0.60),h	1.0	110	5	12.3	6850	103	0.88	3.5
22036+5306	5.5	B⋆(0.80)cw(b),an,ps(s,an),h	4.0	255	6.5	7	8850	35−50	23.5	2
22223+4327	17.5	Ec⋆(0.43),h(a)	1.5	205	7.5	14	11000	99	0.79	4.3
23304+6147	5.2	Mc⋆(0.60),ps(m),h(a)	1.1	145	5.5	15.5	7000	99	0.82	4.2

NOTE.—Numbers in parentheses imply *assumed* values.
[a] Values of r_{AGB}, t_{AGB}, M_d, and distance are from Vinkovic et al. (2004).
[b] Values of parameters are from Sánchez Contreras et al. (2007), scaled appropriately for $L = 6000 L_\odot$ as necessary.
[c] Values of parameters are from Sahai et al. (2007a) and Sánchez Contreras et al. (2006), scaled appropriately for $L = 6000 L_\odot$ as necessary.

TABLE 4
Properties of Previously Observed, Well-Resolved Preplanetary Nebulae

IRAS Name	F_{25}/F_{12}	Imaging Refs.	Chem.[a]	Morphology
Well-Studied PPNs				
AFGL 618[b]	2.3	1	C	Mcw,ml,h(e,a)
Red Rectangle	1.1	2	C+O	Bow
OH 231.8+4.2	11.9	3	O	Bcw,sk
07131−0147	1.6	4	O	Bow★(0.54)
Frosty Leo Neb.	>17	5	O	Bcw(b)★(0.60),an,ml,ps(m,an,s)
Roberts 22	5.5	6	C+O	Bcw,ml,ps(s),h(e)
Hen 3-401	9.3	7	C	Bow★(0.60),sk
Boomerang Neb.	1.3	8	...	Bow★(0.54)
16342−3814	12.3	9	O	Bcw,ps(s)
Hen 3-1475	4.0	10	O	Bow(b)★(0.55),an,sk,ps(an,s),h
M1-92	3.4	11	O	Bcw(b)★(0.55),an
AFGL 2688	...	12	C	Bcw(b),ml,h(e,a,sb)
Less Well-Studied PPNs				
02229+6208	3.1	10	C	E★(0.55)
04296+3429	3.6	13	C	Bcw(b),h
05341+0852	2.2	10	C	Ec★(0.55),ps(s),h
06530−0213	4.5	10	C	Bc★(0.55),ml,ps(s),h(e)
07134+1005	4.8	10	C	Ec★(0.41),h(e)
07430+1115	3.9	10	C	E★(0.55),h
08005−2356	2.9	10	O	Bo★(0.55)
16594−4656	6.6	14	C	Mcw★(0.60),an,ps(m,an),h(a)
17106−3046	15.5	15	O	Bw(b)★(0.60)
17150−3224	5.6	16, 19	O	Bcw★(1.6),h(a,sb)
17245−3951	13.3	14, 19	O	Bcw★(1.6),h(sb)
1743+5003	30.1	10	O	Ec★(0.41)
17441−2411	4.5	17, 19	C	Bcw★(1.6),h(e,a)
18095+2704	2.8	10	O	Bc,h
19374+2359	4.2	10	O	B,h(e)
19477+2401	4.9	14	C	E,h(e)
20028+3910	5.0	18	C	Bcw(b),h(e,a,sb)
22272+5435	4.1	10	C	Ec★(0.55),h(a)
22574+6609	3.3	14	C	Bwh(i)
23321+6545	6.3	10	C	Ec

[a] Information about the nebular chemistry has been taken either directly (in most cases) from the imaging reference paper or from papers cited in the latter.

[b] The "a" descriptor is based on an unpublished *HST* ACS F606W image provided by B. Balick (J. Huehnerhoff et al. 2008, in preparation) using data from GO 9430 (PI: S. Trammell).

References.— (1) Lee & Sahai 2003; (2) Cohen et al. 2004; (3) Bujarrabal et al. 2002; (4) Scarrott et al. 1990 (ground-based image only); (5) Sahai et al. 2000a; (6) Sahai et al. 1999c; (7) Sahai et al. 1999a; (8) Sahai et al. 2000b; (9) Sahai et al. 1999b; (10) Ueta et al. 2000; (11) Bujarrabal et al. 1998; (12) Sahai et al. 1998a; (13) Sahai 1999; (14) Su et al. 2001; (15) Kwok et al. 2000; (16) Kwok et al. 1998; (17) Su et al. 1998; (18) Hrivnak et al. 2001; (19) Su et al. 2003.

in a luminosity of 2600 $L_\odot$, we have scaled up the distance-dependent values given in Table 3 appropriately from the values given by Sahai et al. (2005). IRAS 19024 shows OH maser emission and is therefore O-rich.

IRAS 19134+2131.—This object belongs to the class of "water-fountain" nebulae—PPNs with very high speed jets seen in H_2O maser emission. IRAS 19134 appears quite compact in the optical images but is clearly elongated along P.A. = $\sim 94°$ (Fig. 16), which is consistent with the orientation of the bipolar H_2O jet (Imai et al. 2004, 2007). In spite of the limited resolution, there appear to be two lobes separated by an intensity minimum; hence, we tentatively classify this as a bipolar object with closed lobes and a waist. No significant halo was detected for this source.

IRAS 19292+1806.—This object shows a bipolar shape (Fig. 17). A faint elliptical halo can be seen in the F814W image. If the halo is due to a spherical AGB mass-loss envelope, the elliptical shape indicates that the AGB envelope is being indirectly illuminated by the lobes, or that light from the central source

cannot get out to the larger distances at low latitudes. By azimuthal averaging, this halo can be traced out to a radius of 2.5″. Using an AGB envelope expansion velocity of 10.5 km s^{-1} derived from OH maser data, we find that $t_{AGB} = 4250(D_L/5.2$ kpc) yr.

IRAS 19306+1407.—This object shows a bipolar shape, with roughly cylindrical lobes (Fig. 18). The central star (spectral type B0:e; SIMBAD database) is directly visible, and the lobes are surrounded by a tenuous round halo. By azimuthally averaging, the halo can be traced out to a radius of $\sim 4''$; the radial distribution follows a power law, $r^{-\beta}$, where $\beta \sim 3.3$. No OH maser data are available for this source. This source most likely has a mixed chemistry (i.e., shows both carbon- and oxygen-rich dust features): Hrivnak et al. (2000) find PAH features in its *ISO* spectra, and Hodge et al. (2004) find silicate features at 11, 19, and 23 μm. We have determined an AGB expansion velocity of 14 km s^{-1} from our OVRO CO $J = 1-0$ survey (Sánchez Contreras & Sahai 2003) for this object, signifying that the AGB envelope was characterized by a roughly constant mass-loss rate over a period

$t_{\mathrm{AGB}} = 6650(D_L/4.9 \text{ kpc})$ yr. Lowe & Gledhill (2007) find a dust mass of $(8.9 \pm 5) \times 10^{-4} \ M_\odot$ using a distance of 2.7 kpc from detailed modeling. Their value, when scaled by the square of the ratio of our larger distance to theirs, i.e., $(4.9/2.7)^2$, gives a dust mass of $(2.9 \pm 1.6) \times 10^{-3} \ M_\odot$, which is larger than, but consistent within uncertainties with, our value of $1.3 \times 10^{-3} \ M_\odot$ (Table 3).

IRAS 19475+3119.—A detailed multiwavelength study of this object, including *HST* imaging, has been reported by Sahai et al. (2007a), and an interferometric study of millimeter-wave CO line emission has been carried out by Sánchez Contreras et al. (2006). Hence, we briefly summarize the main characteristics here. IRAS 19475 (F3 Ib central star; SIMBAD database) has a quadrupolar shape (Fig. 19) showing two bipolar elongated lobes emanating from the center of the nebula. One of the bipolar lobe pairs clearly shows detailed point-symmetric structure with respect to the central star. A faint, surface-brightness-limited, diffuse halo surrounds the lobes. Since Sahai et al. (2007a) assumed a far kinematic distance of 4.9 kpc, at which this object has a luminosity of $8300 \ L_\odot$, we have scaled the values given by Sahai et al. (2007a) for the distance-dependent parameters given in Table 3 appropriately. For the dust mass, we use the study of Sarkar & Sahai (2006), and we exclude the additional mass of large, cold grains derived from submillimeter-wave/millimeter-wave data for this object by Sahai et al. (2007a). The *ISO* spectra of IRAS 19475 show that it is O-rich (Sarkar & Sahai 2006).

IRAS 20000+3239.—This object is roughly elliptical in shape and is surrounded by a prominent round halo (Fig. 20). The radial brightness distribution in the halo can be roughly described by a segmented power law, with an inner region extending to a radius of $\sim 2''$ described with a power-law index $\beta \sim 2.3$ and an outer region which can be traced to a radius of about $5''$ and a power-law index $\beta \sim 4.2$. The age of the AGB envelope is $6850(D_L/3.5 \text{ kpc})$ yr. The central star is classified as G8 Ia, and the *ISO* SWS spectra show it to be a C-rich object (Hrivnak et al. 2000).

IRAS 22036+5306.—Since a detailed multiwavelength study of this O-rich PPN, which has an overall bipolar morphology (and an F5 [or earlier] central star), has been reported by Sahai et al. (2003), we briefly summarize the main characteristics here. The ACS images of this extended bipolar nebula (Fig. 21) show the main structures previously imaged with WFPC2 (Sahai et al. 2003), namely, the bipolar lobes with bright regions S1 and S2, the central ringlike dense waist (R_b and R_d), and the knotty linear structures labeled J_E and J_W in Sahai et al. (2003). In addition, the F814W image resolves the central star from the surrounding bright nebulosity and shows the presence of two ansae just beyond the tips of the main lobes, as well as a faint round halo. The radial brightness distribution follows a segmented power law, with an inner region described with a power-law index $\beta \sim 2.3$ and extending to a radius of about $\sim 3''$ and an outer region described by a power-law index $\beta \sim 4.4$, which can be traced to a radius of about $6.5''$. Sahai et al. (2003) argue for a distance of 2 kpc for this object, at which its luminosity is $2300 \ L_\odot$ and the total (dust+gas) mass of the dominant shell component used to model the SED is about $4.7 \ M_\odot$. Given this large mass, and a further large (but uncertain) mass contribution from an additional cold component estimated recently from IRAS 22036+5306's submillimeter and millimeter-wave continuum fluxes (Sahai et al. 2006b), it is unlikely that the object can be at the larger distance which corresponds to a luminosity of $6000 \ L_\odot$. Hence, for this object, we have retained a value of 2 kpc for its distance. We derive $t_{\mathrm{AGB}} = 8850(D_L/2 \text{ kpc})$ yr assuming an AGB expansion velocity of 7 km s^{-1} (derived from the central narrow component of the ^{13}CO line shown by Sahai et al. 2006a).

IRAS 22223+4327.—This object has a central round core, with two small lobes protruding on the southern side and a single small lobe protruding on the northern side (Fig. 22). A prominent, smooth halo surrounds the central aspherical nebula. Faint, thin, partial shells can be seen within the halo in the F435W image and, to a lesser extent, in the F606W image. These structures cannot be fitted with concentric circles around the central star. Radial streaks due to the PSF of the central star are also present. The central star is classified as G0 Ia in the SIMBAD database. Using azimuthal averaging, one can trace the halo out to a radius of $\sim 7.5''$; the radial distribution follows a power law, $r^{-\beta}$, where $\beta \sim 3.8$, signifying that the AGB envelope is characterized by an increasing mass-loss rate over a period of $11,000(D_L/4.3 \text{ kpc})$ yr. The CSE is classified as C-rich, since it shows millimeter-wave HCN emission (Omont et al. 1993). The CO profile shows weak line wings extending over 50 km s^{-1}, indicating the presence of a fast post-AGB outflow.

IRAS 23304+6147.—The object probably has a quadrupolar shape, although the two pairs of lobes are not as well separated as, e.g, in IRAS 19475+3119. We tentatively classify it as M. The lobes are surrounded by a prominent round halo (Fig. 23). The radial distribution in the halo can be roughly described as a segmented power law, with an inner region extending to a radius of about $\sim 2.5''$ described with a power-law index $\beta \sim 2.5$ and an outer region which can be traced to a radius of $\sim 5.5''$ and a power-law index $\beta \sim 3.8$. The age of the AGB envelope is $7000(D_L/4.2 \text{ kpc})$ yr. The central star is visible and is classified as G2 Ia in the SIMBAD database. It has molecular carbon absorption features and is therefore C-rich (Hrivnak 1995). This object is thus remarkably similar to IRAS 20000+3239 in the properties of its post-AGB and AGB ejecta, except for its primary morphological classification, which is M, whereas IRAS 20000+3239 is E.

4.1. Related Objects: Nascent Preplanetary Nebulae and Young Planetary Nebulae

We included a few objects in our survey which, from the evolutionary standpoint, bracket the preplanetary evolutionary phase, the main focus of our survey. Thus, we included two very late AGB stars, one which is O-rich (IRAS 01037+1219, also WX Psc, IRC+10011) and another which is C-rich (IRAS 23166+ 1655, AFGL 3068). Our observations of IRAS 01037+1219 show a central, asymmetrical, elongated (oval-shaped) nebulosity in the F814W image. The object appears much fainter and more compact in the F606W image (Fig. 24). The peak brightness region is also elongated and nonstellar (Fig. 25). The position angles of the elongations seen on small (Fig. 24) and large scales (Fig. 25) are different, suggesting that a fast collimated outflow whose axis is changing is responsible for the elongation. We believe that this object has just begun the transition to the PPN phase, and we label it a "nascent PPN," or nPPN. The distance and dust-shell-related parameters (Table 3) for IRAS 01037 are taken directly from the detailed modeling study by Vinkovic et al. (2004) and have not been rescaled to our standard luminosity value of $6000 \ L_\odot$.

Other well-studied objects which belong to the nPPN class include the carbon stars IRC 10216 (Skinner et al. 1998), CIT-6 (Schmidt et al. 2002), and V Hydrae (Sahai et al. 2003), all of which show strongly aspherical structures at their centers; a brief summary of an *HST* survey directed at this class is given by Sahai et al. (2006a). A detailed discussion of this class of objects is deferred to a future paper.

IRAS 23166+1655 does not show any bright central nebulosity or a central star; however, there is a substantial diffuse

round halo with a large number of roughly circular arcs centered on the 2MASS coordinates of this object. The arcs and their interpretation have been discussed by Mauron & Huggins (2006) and Morris et al. (2006). Since there is no central organized structure, this object is not relevant for our morphological classification system.

We also included four young PNs, IRAS 17047−5650 (better known as CPD −56 8032), IRAS 21282+5050, IRAS 22568+6141 (Garcia Lario et al. 1991), and IRAS 19255+2123 (better known as K3-35), in our survey. IRAS 17047−5650 is a well-known dusty PN with a late-WC central star (Crowther et al. 1998). Its F435W image (Fig. 26) shows a multipolar object with one well-defined set of diametrically opposed bipolar lobes oriented roughly along a northeast-southwest axis; in a second pair oriented north-south, the northern lobe is observable to its tip, but the southern counterpart appears to be surface-brightness-limited along its length, and its tip is not seen. There are complex brightness variations which likely represent additional geometric structures; e.g., one may infer the presence of a shell oriented roughly along a northwest-southeast axis. The central star is visible in the image.

The PN IRAS 21282+5050 (Crowther et al. 1998) shows a morphology (Fig. 27) qualitatively very similar to that of CPD −56 8032: it has two pairs of diametrically opposed lobes and a central roughly rhomboidal shell. Our F606W image of IRAS 22568+6141 (Fig. 28) shows a bipolar nebula with highly structured lobes; no central star can be seen. A compact bright ansa can be seen just south of the southeastern lobe, and it appears to be connected to this lobe via a narrow, jetlike feature. A counterpart to this elongated feature is seen marginally just north of the northwestern lobe. The overall shape of the lobes is roughly point symmetric.

IRAS 19255+2123 is a well-studied dusty PN noted for being the first PN in which H_2O maser emission was found (Miranda et al. 2001); such PNs are exceedingly rare, presumably due to the very short lifetime of H_2O masers during the PN phase. Its F606W image shows a bipolar nebula (Fig. 29); the north lobe, which is the brighter of the two, shows significant brightness structure, including a bright region on its eastern periphery (B_N), that has a bright point-symmetric counterpart in the southern lobe (B_S). A bright ansa is seen at the tip of the southern lobe (A_S), with a possible counterpart at the tip of the northern lobe (A_N). A dense, dusty waist separates the two lobes, and a diffuse halo surrounds the lobes at low and intermediate latitudes.

4.2. IRAS 05506+2414: An Unrelated Object?

The morphology of this object is unlike that of any PPN or PN, although it meets the selection criteria for our survey. The *HST* image (Fig. 30) shows a bright compact knot (Sa) and a fanlike spray of elongated nebulous features (e.g., knots K1−4; not all the knots seen in the image have been labeled) which are separated from the former but appear to emanate from it. A second compact knot (Sb) is seen to the west of the main source. We find that the *MSX* and 2MASS sources identified with the *IRAS* source are located at the position of knot Sa, indicating that it is associated with the stellar source powering an outflow that produces knots K1−4.[10] A 1612 MHz OH maser source was discovered toward IRAS 05506 with the Arecibo dish (Chengalur et al. 1993); the profile is not the typical double-peaked profile seen toward most dying stars. The main lines at 1665, 1667 MHz were detected by Lewis (1997) with peak fluxes of 300 and 150 mJy using Arecibo; the emission covers about 15 km s^{-1} in the 1612 MHz line and ∼40–45 km s^{-1} in the main lines.

---

[10] These knots are most likely Herbig-Haro objects.

If IRAS 05506 is not associated with an evolved star, but instead is a young stellar object (YSO), then the OH maser observations argue for it not being a low-mass YSO, since there are no known OH masers toward low-mass YSOs. So, if it is a YSO, it must be related to a high-mass star formation region (SFR), suggesting the presence of an ultracompact H II region with detectable continuum emission. However, the NRAO VLA Sky Survey at 20 cm shows no continuum source toward IRAS 05506 down to an rms noise of ∼400 μJy beam^{-1}. Could IRAS 05506 then really be a PPN, but with a morphology which has never been seen before in PPNs or PNs? While this is an improbable hypothesis, it is not implausible, considering that not so long ago, Sahai & Nyman (2000) discovered a PN with a bipolar, knotty jet, bearing an uncanny resemblance to jets seen in low-mass YSOs. A detailed discussion of the nature of IRAS 05506 is outside the scope of this paper but will be presented, together with new optical, millimeter-wave, and radio data, in a forthcoming paper (Sahai et al. 2007b).

5. DISCUSSION

The morphological scheme we have presented in this paper is based on the PPNs in our survey and on additional well-studied PPNs outside our sample. Our PPN survey sample is a well-defined sample, but it is not a complete sample. We have listed in Table 4 all PPNs with high-resolution images in the literature outside our sample, and we find that all of these can be accommodated within our classification scheme. Thus, Tables 3 and 4 list all known galactic PPNs with existing high-resolution images—a total of 53 objects. Many of the objects in Table 4 are taken from the PPN survey by Ueta et al. (2000). These authors classify PPNs as either SOLE (objects with a bright central star embedded in a faint extended nebulosity) or DUPLEX (objects with bipolar shapes with a completely or partially obscured central star) and suggest that the *axisymmetry* in PPNs is created by an equatorially enhanced superwind at the end of the AGB phase. In view of the many very strong departures from axisymmetry in a very significant fraction of the full sample of PPNs, we do not think that the Ueta et al. classification provides a sufficiently complete framework for classifying the morphologies of PPNs.

5.1. Preplanetary and Young Planetary Nebulae: Morphological Similarities

The wide variety of morphologies we have found are qualitatively similar to those found for young PNs in two previous *HST* surveys (GO 6353 and 8345), in which a total of 65 objects were imaged (e.g., Sahai & Trauger 1998; Sahai 2000, 2003; Sahai et al. 2000), and other ground-based studies. In particular, we find multipolar objects like IRAS 19024+0044, which closely resembles the "Starfish Twins"—two young PNs with multiple lobes (Sahai 2000). The quadrupolar object, IRAS 19475+3119, probably belongs to the class of quadrupolar PNs first identified by Manchado et al. (1996). In the "bipolar" class, the cylindrical lobe shape, together with the associated very dense waist found in IRAS 13428−6232, is very similar to that of the well-studied PN IC 4406 (e.g., Sahai et al. 1991). The (bipolar) hourglass-shaped PPN, IRAS 15452−5459, resembles hourglass-shaped PNs like MyCn 18 (Sahai et al. 1999d) and Hb 12 (Sahai & Trauger 1998).

There are a few PPNs which are best described as elongated (class E). If the elongated morphology of these objects is due to their having prolate ellipsoidal shapes, then we expect that they will evolve into the category of PNs which have been classified as elliptical in morphological schemes for PNs (e.g., Corradi &

Schwarz 1995). Alternatively, these class E objects may be intrinsically bipolar but with the pinched-in appearance of the lobes at their bases not being apparent, because either (1) the polar axis is sufficiently tilted toward us, or (2) they are insufficiently resolved. A good example of possibility 1 is provided by IRAS 18420−0512 (Fig. 14), where the northwestern lobe shows some evidence for being pinched-in on its northeastern periphery. As in the case of our surveys of young PNs with *HST* (Sahai & Trauger 1998; Sahai 2003), we found no round PPNs.

The similarity in morphologies between all PPNs observed with high spatial resolution and young PNs qualitatively indicates that (1) the former are the progenitors of aspherical PNs, and (2) the onset of aspherical structure begins during the PPN phase (or earlier). This suggests that the primary shaping of a PN clearly does not occur during the PN phase via the fast radiative wind of the hot central star, but significantly earlier in its evolution.

The morphological system for PPNs which we have presented can be adapted for young PNs directly. The broadband optical (and near-infrared) images of PPNs show light scattered off dust grains in the circumstellar material. The interaction of the fast collimated wind from the central star of the PPN with the slowly expanding, spherical, AGB mass-loss envelope produces lobes with dense walls which consist mostly of swept-up AGB wind material. The walls are overdense with respect to both the interiors and the exteriors of the lobes. The shapes of the nebular lobes, which are the brightest regions of PPNs, thus represent the shapes of the dense walls of the lobes, since the interiors of the lobes are tenuous, as demonstrated by the frequent presence of limb brightening in the lobes. This basic structure of the lobes in PPNs is reproduced in numerical simulations by Lee & Sahai (2003).

When the central star becomes hot enough to substantially ionize the circumstellar material, the nebular walls then appear as bright features in Hα and forbidden-line emission (e.g., [N II] $\lambda\lambda$6548, 6583). Note that because the optical-line emission is proportional to $n_e^2 l$, and thus, $n^2 l$ (where n_e and n are the electron and total density and l is the path length), whereas scattered-light intensity is proportional to nl, generally the brightness contrast between the nebular walls and their surroundings is likely to be higher for PNs than for PPNs. The lobe morphology, in both the PPN and PN phases, is a direct indicator of the geometric shapes of the dense lobe walls, and therefore of the wind-wind interaction process which created them.

The only distinction which needs to be kept in mind when modifying the PPN classification scheme for PNs is related to the appearance of the waist region. Since most surveys of PNs have been carried out in emission-line filters, the waist quite often (but not always) appears as a bright feature, rather than a dark feature. Hence, unlike the case of PPNs, in our classification of young PNs, we will not define the waist in terms of a minimum in intensity along the long axis of the nebula. Indeed, the waist is often the brightest structural component of a bipolar or multipolar PN, which is understandable if we assume that the waist region has much more mass than the lobes. Note also that if the waist region is in expansion, then it will continue to flow radially outward from the star as a PPN evolves into a PN. The central regions of PNs with waists are thus, in general, expected to be more exposed and visible than those of the PPNs from which they evolve. Of course, very young PNs such as IRAS 22568+6141 (Fig. 28) and K3-35 (Fig. 29) still have optically thick waists fully or partially obscuring their central stars. A detailed morphological classification of the young PNs from the *HST* surveys described in Sahai & Trauger (1998) and Sahai (2003), which are presumably most closely related to PPNs in an evolutionary sense, will be

presented in a future paper (R. Sahai & M. Morris 2008, in preparation).

5.2. *Morphology and Nebular Chemistry*

The "total" sample of PPNs with resolved morphologies listed in Tables 3 and 4 (our survey plus previously observed ones) includes objects with both oxygen-rich and carbon-rich chemistries, as well as a few which display mixed chemistry (i.e., show features representative of both carbon-rich and oxygen-rich chemistry). Although O-rich objects outnumber the C-rich ones, there is a substantial fraction of the latter (about 25%). Since the ratio of dusty O-rich stars to dusty C-rich stars, as estimated from a sample drawn from the *IRAS* PSC, is about 9 (Thronson et al. 1987), and these objects are presumably the progenitors of dusty PPNs, C-rich PPNs are certainly not underrepresented in our total sample of PPNs relative to their parent population. Within the total PPN sample, there does not appear to be any significant correlation of morphology with nebular chemistry.

5.3. *Lobes*

The variety of lobe shapes and structures seen in young PNs led to a new model by Sahai & Trauger (1998) for PN shaping in which fast collimated outflows, operating during the PPN or very late AGB phase, are the primary agents in producing aspherical PNs. Hence, our morphological classification system puts considerable emphasis on including descriptors which are related to the shapes, structures, and symmetries of the lobes.

An important example of this emphasis is the fairly detailed characterization of point symmetry in our classification scheme, based on the recognition that various subtypes of point symmetry impose fairly strong constraints on specific formation mechanisms. This has been discussed in detail by Sahai et al. (2005) in a study of the PPN IRAS 19024+0044. Briefly, the M and ps(m) classification of this object suggests a precessing *bipolar* jet, in which the fast outflow could be in the form of discrete blobs ejected in discontinuous episodes, or a high-velocity jet that discontinuously changes direction, leading to the sculpting of multiple lobes in different directions within the ambient AGB envelope. The presence of point-symmetric ansae at the tips of one of the lobe pairs, represented by the ps(an) descriptor, requires the collimated outflow which produced these lobes to have changed its axis during its operation, although by much less than the angular separation between lobes. Thus, the physical mechanism(s) which produces the collimated outflows must be able to accommodate two different timescales, one associated with generating the point-symmetric ansae within a lobe pair and one associated with generating the point-symmetrically distributed multiple lobes.

The "o" and "c" secondary classifiers (related to whether lobes are open or closed at their ends, respectively) provide another example of descriptors that raise some important questions related to the dynamical interactions believed to shape PPNs. Generally, post-AGB collimated winds or jets interacting with AGB CSEs (e.g., Lee & Sahai 2003) will produce closed lobes as the fast wind sweeps up the ambient CSE material in front of it. If the density of the ambient material falls sufficiently rapidly with radius (e.g., as r^{-3} or more steeply, perhaps even in a discontinuous manner), and/or the fast wind turns off, reducing the ram pressure compressing the dense material at the tip of the lobe, the compressed layer will expand due to thermal pressure.[11] Second, fragmentation of the compressed layer due to hydrodynamic

---

[11] Note, however, that since this material cools rapidly, the consequently relatively low sound speed compared to the much higher expansion speed will limit the efficacy of this effect.

instabilities may also occur. As a result of the above two effects, the end of the lobe could dissipate and become undetectable, leading to the open-lobe appearance. The bipolar PPN Hen 3-401, which shows lobes with tattered ends (Sahai et al. 1999d), is a possible example of fragmentation of the lobe ends due to instabilities. But hourglass-shaped bipolar PPNs such as IRAS 13557 (Fig. 4) and IRAS 15452 (Fig. 6), which have wide-open ends, show no obvious evidence of fragmented clumpy material. Furthermore, if "c" lobes evolve into "o" lobes over time, then we would expect the former to have systematically smaller values of t_{PAGB} than the latter, but this does not seem to be the case from an inspection of our results in Table 3 (note, however, that our sample is still too small to make this a robust conclusion). Perhaps magnetic fields stabilize the lobe walls against fragmentation in some objects and not others, depending on the field strength and configuration. To summarize, a theoretical investigation of issues related to the formation of open and closed lobes using, e.g., numerical hydrodynamic simulations is thus quite important for our general understanding of the formation of aspherical structure in PPNs.

5.4. Halos

The prominent halos surrounding the central aspherical shapes seen in many of our objects are direct signatures of the undisturbed CSEs of the progenitor AGB stars. The halos generally have round or elongated shapes. It is quite plausible that objects with elongated halos have AGB envelopes which are intrinsically round but appear elongated, because they are either being indirectly illuminated by the lobes or the light from the central source cannot get out to the larger distances at low latitudes. The majority of these have surface brightness distributions consistent with a constant mass-loss rate with a constant expansion velocity (e.g., IRAS 17253−2831, IRAS 17440−3310, IRAS 18420−0512, and IRAS 19024+0044). But there are also examples of objects with varying mass-loss rates, with instances where the mass-loss rate was both higher (IRAS 23304+6147) and lower (e.g., IRAS 19475+3119) in the past.

Three objects (IRAS 20000+3239, IRAS 22036+5306, and IRAS 23304+6147) show halos which require a two-piece segmented power law to describe the surface brightness. This implies somewhat discontinuous changes in the AGB mass-loss rate, if we assume that the envelope expansion velocity has remained constant.[12] Comparing the three objects, we find the interesting result that in all of these, the power law in the outer (inner) region is steeper (shallower) than that for a constant mass-loss rate. The implication is that for these objects, the mass-loss rate went through a maximum, first increasing over a period of ∼3800–4800 yr, and then decreasing.

5.5. Waists

A significant fraction of PPNs appear to have an optically thick concentration of dust in their equatorial plane, i.e., a waist. We refer to this dust distribution as a disk, setting aside the question of whether it is a bound, orbiting disk or an equatorial concentration of dust in an outflowing wind. We have noted in our classification scheme that, in quite a few PPNs, the disk has a sharp radial edge, that is, a discontinuity in the extinction projected against the extended emission from the reflection
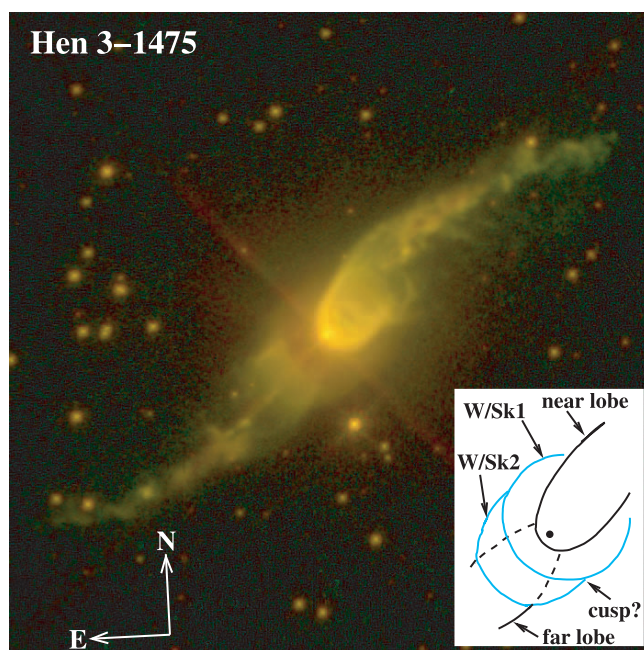
FIG. 31.—Color-composite (*green*, F555W; *red*, F814W) *HST* image of the PPN Hen 3-1475 (18.2″ × 18.2″). The inset is a schematic of the central region, showing the outlines of the main structural features; background/shadowed features are shown as dashed curves. The cyan curves show the waist/skirt features, whereas the black curves show the bipolar lobes.

nebula.[13] The curvature of this discontinuity is typically convex relative to the nebula's center of symmetry, consistent with its being caused by radial structure in an axisymmetric disk.

This result carries interesting implications about the geometry of the disk. For the simple case of a bipolar nebula, for example, a sharp edge projected against the far lobe is a strong indication that the disk is density-bounded at its outside edge. The sharp edge to the waist in that case is most likely due to the abrupt radial termination of the disk. If the surface density of dust in the disk were to fall off monotonically without an abrupt falloff (e.g., as $1/r$ for a disk that is radially outflowing at constant velocity and constant mass loss rate), then the edge would be relatively diffuse. These remarks apply to a situation in which the disk scale height increases with radius, as would be expected for an outflowing disk. Examples of sharp edges are found in the well-studied PPNs such as AFGL 2688 (Sahai et al. 1998a) and in our sample objects IRAS 19292+1806 (Fig. 17) and IRAS 22036+5306 (Fig. 21).

Determination of which lobe of a bipolar nebula is the far lobe can be done by appeal to the kinematics; the rear lobe is the redshifted lobe. It is usually, although not always, the dimmer or more absorbed lobe because of extinction by the disk, but this is not a reliable indicator because the lobes may be intrinsically asymmetric (e.g., OH 231.8+4.2).

We note that it is possible to have a sharp edge against the near lobe of a bipolar PPN if several conditions are met: (1) the disk has a sharp surface boundary, (2) the scale height of the disk density distribution rises linearly or less rapidly than linearly with radius, and (3) the observer's line of sight is approximately tangent to that surface. The last condition implies that the observer is

---

[12] It is unlikely that radial extinction of the illuminating light from the center plays a significant role in establishing a steep power-law index β for the surface brightness in the outer region, because if radial extinction was important, it would have an even more dramatic effect on steepening the power law in the inner region.

[13] Because the waist regions are best seen when they are edge-on or close to edge-on, in which case one cannot determine from the images whether or not the disk is truncated at an outer radius, there is an observational bias against seeing waists with such outer edges.
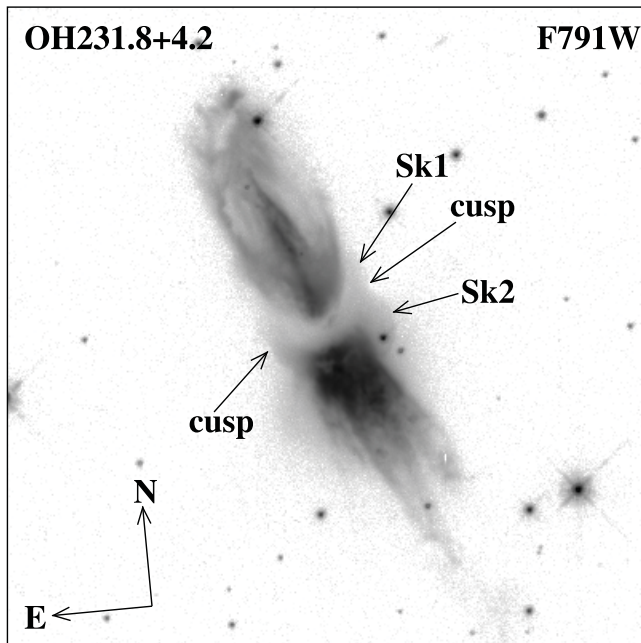
FIG. 32.—*HST* (F791W) image of the PPN OH231.8+4.2 ($39.8'' \times 39.8''$).

viewing the system from near the equatorial plane, which, in any case, is the best vantage point from which to identify such a system as a bipolar or multipolar nebula.

It is also possible for the disk geometry to be arranged so that it gives a sharp edge against the far lobe even if the disk does not have a sharp outer boundary. The conditions for that, however, are quite restrictive: (1) a sharp disk surface boundary, (2) a disk scale height that reaches a maximum at some radius at which the disk is still optically thick, and (3) that the observer's line of sight is tangent to the disk at the point where the disk reaches its maximum scale height. While this is possible, it is not well-motivated physically, so we regard any object that shows a sharp radial edge projected against the far lobe as a case in which the disk has a sharp outer boundary.

The inferred sharp outer boundary to the disks in a number of systems can most easily be explained by an abrupt transition in mass-loss geometry from spherically symmetric to axisymmetric geometry having some combination of a latitude-dependent mass-loss rate and a latitude-dependent outflow velocity. Models for such a transition can be based on the presence of a close binary companion (e.g., Morris 1987, 1990) or on the emergence of a strong stellar magnetic field after mass loss has stripped away enough of the overlying stellar atmosphere (Blackman et al. 2001a, 2001b). These issues will be discussed in a separate paper.

It is important to note that waists with sharp outer edges may not be distinguishable from skirt structures if the nebular axis is sufficiently inclined toward us. An example of this is provided by Hen 3-1475 (Fig. 31). A color figure combining images taken through the F555W and F814W filters with WFPC2 clearly demarcates the waist/skirt structure, most prominently defined by a relatively red, sharp-edged elliptical band (labeled "W/Sk1" in the inset of Fig. 31) which cuts sharply across the southeast or far lobe. Southeast of W/Sk1, one can see a bluer structure whose outer edge is a partial ellipse (W/Sk2 in the inset) which joins W/Sk1 near the equatorial plane. An apparent cusp can be seen on the southwest side of the nebula where W/Sk1 and W/Sk2 meet, suggesting a skirt structure for these features. However, since this cusp feature is not well defined, and its counterpart on the northeast

side is not apparent, we cannot definitively argue for the presence of a skirt in Hen 3-1475.

The central obscuring structure in OH231.8+4.2 (Fig. 32) is quite similar to that of Hen 3-1475, with its near side seen as an obscuring elliptical band, partially cutting across the southwest nebular lobe and partially seen as a bright structure projected against the sky background (labeled "Sk1"). Its far-side counterpart is seen most clearly as a bright structure against the sky background on the eastern and western flanks of the bright southeastern nebular lobe (Sk2). The skirt shape can be inferred from the cusp resulting from the intersection of the projected edges of Sk1 and Sk2 on the northwestern side of the nebula; a similar cusp can be seen somewhat less clearly on the southeastern side. A quantitative analysis of the colors in the central region of these objects may help in better elucidating the structural relationship between the waist and skirt features.

6. CONCLUSIONS

Using the *Hubble Space Telescope*, we have carried out a survey of a well-defined set of candidate preplanetary nebulae (PPNs). We present images of 22 new PPNs and 1 nascent PPN with well-resolved geometric structures. Combining this sample of PPNs with previously studied objects in this class, we have devised a comprehensive new morphological classification system for this class of objects. We summarize our major findings below:

1. We have found a wide variety of aspherical morphologies which include bipolar and multipolar shapes, many of which display point symmetries by virtue of their shapes and/or structures. This variety of morphologies is qualitatively similar to those found for young planetary nebulae (PNs) in previous surveys. As in the case of our surveys of young PNs, we found no round PPNs.

2. We also find prominent halos surrounding the central aspherical shapes in many of our objects; these are direct signatures of the undisturbed circumstellar envelopes of the progenitor AGB stars. The majority of these have surface brightness distributions consistent with a constant mass-loss rate at a constant outflow velocity. But three objects require a segmented power law to describe the surface brightness, indicating that in these objects, the AGB mass-loss rate went through a maximum, first increasing over a period of $\sim$3800–4800 yr and then decreasing.

3. We have estimated the physical sizes of the aspherical nebulae and the halos. Distances have been derived by measuring the bolometric flux of each object from its SED and using a fixed luminosity of 6000 $L_\odot$. A timescale for the duration of the post-AGB mass loss (t_{PAGB}) and a lower limit to the timescale for AGB mass loss (t_{AGB}) have been derived from the expansion ages of the aspherical nebulae and the halos, respectively, by making simplifying assumptions about the expansion speeds of the nebular material. A rather wide range of timescales is found in both cases: t_{PAGB} lies in the range 30–1660 yr, with a median age of 180 yr, and t_{AGB} lies in the range 300–14,700 yr, with a median age of 6650 yr.

4. We have computed dust masses by fitting the SED of each object from the near-infrared (K band) to the far-infrared (as defined by *MSX* and *IRAS* fluxes) using a simple multicomponent model. The mass of the coolest component dominates the mass budget for each object. The dust masses cover the range $(0.53-23.5) \times 10^{-3}$ $M_\odot$; the corresponding total masses, assuming a typical gas-to-dust ratio of 200, are 0.1–4.7 $M_\odot$.

5. No obvious correlations are discernible between the morphologies and the post-AGB ages, dust masses, temperatures, or nebular chemistry.

6. The similarities in morphologies between our survey objects and young PNs support the view that the former are the progenitors of aspherical PNs, and the onset of aspherical structure begins during the PPN phase (or earlier). This suggests that the primary shaping of a PN does not occur during the PN phase via the fast radiative wind of the hot central star, but significantly earlier in its evolution.

REFERENCES

Bakker, E. J., Lamers, H. J. G. L. M., Waters, L. B. F. M., & Waelkens, C. 1996, A&A, 310, 861
Blackman, E. G., Frank, A., Markiel, J. A., Thomas, J. H., & Van Horn, H. M. 2001a, Nature, 409, 485
Blackman, E. G., Frank, A., & Welch, C. 2001b, ApJ, 546, 288
Bowers, P. F., Johnston, K. J., & Spencer, J. H. 1983, ApJ, 274, 733
Bujarrabal, V., Alcolea, J., Sahai, R., Zamorano, J., & Zijlstra, A. A. 1998, A&A, 331, 361
Chengalur, J. N., Lewis, B. M., Eder, J., & Terzian, Y. 1993, ApJS, 89, 189
Cohen, M., Van Winckel, H., Bond, H. E., & Gull, T. R. 2004, AJ, 127, 2362
Corradi, R. L. M., & Schwarz, H. E. 1995, A&A, 293, 871
Crowther, P. A., De Marco, O., & Barlow, M. J. 1998, MNRAS, 296, 367
de Gregorio-Monsalvo, I., Gómez, Y., Anglada, G., Cesaroni, R., Miranda, L. F., Gómez, J. F., & Torrelles, J. M. 2004, ApJ, 601, 921
Garcia Lario, P., Manchado, A., Riera, A., Mampaso, A., & Pottasch, S. R. 1991, A&A, 249, 223
Hodge, T. M., Kraemer, K. E., Price, S. D., & Walker, H. J. 2004, ApJS, 151, 299
Hoffleit, D., Saladya, M., & Wlasuk, P. 1983, A Supplement to the Bright Star Catalogue (New Haven: Yale Univ. Obs.)
Hrivnak, B. J. 1995, ApJ, 438, 341
Hrivnak, B. J., Kwok, S., & Su, K. Y. L. 1999, ApJ, 524, 849
———. 2001, AJ, 121, 2775
Hrivnak, B. J., Volk, K., & Kwok, S. 2000, ApJ, 535, 275
Hu, J. Y., te Lintel Hekkert, P., Slijkhuis, S., Baas, F., Sahai, R., & Wood, P. R. 1994, A&AS, 103, 301
Imai, H., Morris, M., Sahai, R., Hachisuka, K., & Azzollini, F. J. R. 2004, A&A, 420, 265
Imai, H., Sahai, R., & Morris, M. 2007, ApJ, 669, 424
Jura, M. 1986, ApJ, 303, 327
Kwok, S., Hrivnak, B. J., & Su, K. Y. L. 2000, ApJ, 544, L149
Kwok, S., Su, K. Y. L., & Hrivnak, B. J. 1998, ApJ, 501, L117
Kwok, S., Volk, K., & Bidelman, W. P. 1997, ApJS, 112, 557
Lee, C.-F., & Sahai, R. 2003, ApJ, 586, 319
Lewis, B. M. 1997, ApJS, 109, 489
Likkel, L. 1989, ApJ, 344, 350
Lowe, K. T. E., & Gledhill, T. M. 2007, MNRAS, 374, 176
Manchado, A., Stanghellini, L., & Guerrero, M. A. 1996, ApJ, 466, L95
Mauron, N., & Huggins, P. J. 2006, A&A, 452, 257
Miranda, L. F., Gómez, Y., Anglada, G., & Torrelles, J. M. 2001, Nature, 414, 284
Morris, M. 1987, PASP, 99, 1115
———. 1990, in From Miras to Planetary Nebulae: Which Path for Stellar Evolution?, ed. M. O. Mennessier & A. Omont (Paris: Editions Frontieres), 520
Morris, M., & Reipurth, B. 1990, PASP, 102, 446
Morris, M., Sahai, R., Matthews, K., Cheng, J., Lu, J., Claussen, M., & Sánchez Contreras, C. 2006, in IAU Symp. 234, Planetary Nebulae in our Galaxy and Beyond, ed. M. J. Barlow & R. H. Méndez (Cambridge: Cambridge Univ. Press), 469
Neri, R., Kahane, C., Lucas, R., Bujarrabal, V., & Loup, C. 1998, A&AS, 130, 1
Omont, A., Loup, C., Forveille, T., te Lintel Hekkert, P., Habing, H., & Sivagnanam, P. 1993, A&A, 267, 515
Oppenheimer, B. D., Bieging, J. H., Schmidt, G. D., Gordon, K. D., Misselt, K. A., & Smith, P. S. 2005, ApJ, 624, 957
Preite-Martinez, A. 1988, A&AS, 76, 317
Sahai, R. 1999, ApJ, 524, L125
———. 2000, ApJ, 537, L43
———. 2003, in IAU Symp. 209, Planetary Nebulae: Their Evolution and Role in the Universe, ed. S. Kwok, M. Dopita, & R. Sutherland (San Francisco: ASP), 471

Sahai, R., Bujarrabal, V., Castro-Carrizo, A., & Zijlstra, A. 2000a, A&A, 360, L9
Sahai, R., Bujarrabal, V., & Zijlstra, A. 1999a, ApJ, 518, L115
Sahai, R., Hines, D. C., Kastner, J. H., Weintraub, D. A., Trauger, J. T., Rieke, M. J., Thompson, R. I., & Schneider, G. 1998a, ApJ, 492, L163
Sahai, R., Morris, M., Knapp, G. R., Young, K., & Barnbaum, C. 2003, Nature, 426, 261
Sahai, R., Morris, M., Sánchez Contreras, C., & Claussen, M. 2006a, in IAU Symp. 234, Planetary Nebulae in our Galaxy and Beyond, ed. M. J. Barlow & R. H. Méndez (Cambridge: Cambridge Univ. Press), 499
Sahai, R., & Nyman, L.-A. 2000, ApJ, 538, L145
Sahai, R., Nyman, L.-A., & Wootten, A. 2000, ApJ, 543, 880
Sahai, R., & Sánchez Contreras, C. 2002, BAAS, 34, 1254
———. 2004, in ASP Conf. Proc. 313, Asymmetrical Planetary Nebulae III: Winds, Structure and the Thunderbird, ed. M. Meixner et al. (San Francisco: ASP), 32
Sahai, R., Sánchez Contreras, C., & Morris, M. 2005, ApJ, 620, 948
Sahai, R., Sánchez Contreras, C., Morris, M., & Claussen, M. 2007a, ApJ, 658, 410
Sahai, R., Su, K. Y. L, Kwok, S., Dayal, A., & Hrivnak, B. J. 2000b, in ASP Conf. Ser. 199, Asymmetrical Planetary Nebulae II: From Origins to Microstructures, ed. J. H. Kastner, N. Soker, & S. Rappaport (San Francisco: ASP), 167
Sahai, R., te Lintel Hekkert, P., Morris, M., Zijlstra, A., & Likkel, L. 1999b, ApJ, 514, L115
Sahai, R., & Trauger, J. T. 1998, AJ, 116, 1357
Sahai, R., Wootten, A., Schwarz, H. E., & Clegg, R. E. S. 1991, A&A, 251, 560
Sahai, R., Young, K., Patel, N. A., Sánchez Contreras, C., & Morris, M. 2006b, ApJ, 653, 1241
Sahai, R., Zijlstra, A., Bujarrabal, V., & te Lintel Hekkert, P. 1999c, AJ, 117, 1408
Sahai, R., et al. 1998b, ApJ, 493, 301
———. 1999d, AJ, 118, 468
———. 2007b, AJ, submitted
Sánchez Contreras, C., Bujarrabal, V., Castro-Carrizo, A., Alcolea, J., & Sargent, A. 2006, ApJ, 643, 945
Sánchez Contreras, C., Le Mignant, D., Sahai, R., Gil de Paz, A., & Morris, M. 2007, ApJ, 656, 1150
Sánchez Contreras, C., & Sahai, R. 2004, in ASP Conf. Proc. 313, Asymmetrical Planetary Nebulae III: Winds, Structure and the Thunderbird, ed. M. Meixner et al. (San Francisco: ASP), 377
Sánchez Contreras, C., Sahai, R., Gil de Paz, A., & Goodrich, R. W. 2003, BAAS, 35, 1220
Sarkar, G., & Sahai, R. 2006, ApJ, 644, 1171
Schmidt, G. D., Hines, D. C., & Swift, S. 2002, ApJ, 576, 429
Sevenster, M. N., Chapman, J. M., Habing, H. J., Killeen, N. E. B., & Lindqvist, M. 1997a, A&AS, 122, 79
———. 1997b, A&AS, 124, 509
Sevenster, M. N., van Langevelde, H. J., Moody, R. A., Chapman, J. M., Habing, H. J., & Killeen, N. E. B. 2001, A&A, 366, 481
Sivarani, T., Parthasarathy, M., Garcia Lario, P., Manchado, A., & Pottasch, S. R. 1999, A&AS, 137, 505
Skinner, C. J., Meixner, M., & Bobrowsky, M. 1998, MNRAS, 300, L29
Su, K. Y. L., Hrivnak, B. J., & Kwok, S. 2001, AJ, 122, 1525
Su, K. Y. L., Hrivnak, B. J., Kwok, S., & Sahai, R. 2003, AJ, 126, 848
Su, K. Y. L., Volk, K., Kwok, S., & Hrivnak, B. J. 1998, ApJ, 508, 744
te Lintel Hekkert, P., Caswell, J. L., Habing, H. J., Haynes, R. F., & Norris, R. P. 1991, A&AS, 90, 327
te Lintel Hekkert, P., & Chapman, J. M. 1996, A&AS, 119, 459
te Lintel Hekkert, P., Chapman, J. M., & Zijlstra, A. A. 1992, ApJ, 390, L23
te Lintel Hekkert, P., Habing, H. J., Caswell, J. L., Norris, R. P., & Haynes, R. F. 1988, A&A, 202, L19

Thronson, H. A., Jr., Latter, W. B., Black, J. H., Bally, J., & Hacking, P. 1987, ApJ, 322, 770

Trams, N. R., Lamers, H. J. G. L. M., van der Veen, W. E. C. J., Waelkens, C., & Waters, L. B. F. M. 1990, A&A, 233, 153

Ueta, T., Meixner, M., & Bobrowsky, M. 2000, ApJ, 528, 861

Van de Steene, G. C., van Hoof, P. A. M., & Wood, P. R. 2000, A&A, 362, 984

Vinkovic, D., Blocker, T., Hofmann, K.-H., Elitzur, M., & Weigelt, G. 2004, MNRAS, 352, 852

Zijlstra, A. A., Chapman, J. M., te Lintel Hekkert, P., Likkel, L., Comeron, F., Norris, R. P., Molster, F. J., & Cohen, R. J. 2001, MNRAS, 322, 280

Zijlstra, A. A., te Lintel Hekkert, P., Pottasch, S. R., Caswell, J. L., Ratag, M., & Habing, H. J. 1989, A&A, 217, 157